Computer Methods in Applied Mechanics and Engineering 456 (2026) 118957

Contents lists available at ScienceDirect

Comput. Methods Appl. Mech. Engrg.

journal homepage: www.elsevier.com/locate/cma

Stabilized explicit two-phase material point method for robust solid-fluid coupling in large-deformation porous media

Zhang Cheng [a], Shiwei Zhao [a,b,*], Hao Chen [a], Jidong Zhao [a,*]

[a] Department of Civil and Environmental Engineering, Hong Kong University of Science and Technology, Clearwater Bay, Kowloon Hong Kong SAR, China
[b] Institute of Water Engineering Sciences, Wuhan University, Wuhan, China

ARTICLE INFO

Keywords:
Material point method
Solid-fluid coupling
Weakly compressible fluids
Explicit time integration
Large deformation
Stabilized methods

ABSTRACT

The hydro-mechanical coupling in porous media governs critical engineering processes and disaster prediction. While the Material Point Method (MPM) excels in large-deformation solid-fluid simulations, persistent stress and pressure oscillations undermine accuracy. This study introduces a stabilized explicit two-phase MPM framework for robust solid-fluid coupling in large-deformation porous media, eliminating oscillations without compromising efficiency. Key innovations include: (1) dual volume averaging using high-order B-spline basis functions to suppress fluid pressure oscillations, and (2) hybrid strain smoothing for solid phase stress mitigation. The AFLIP mapping scheme that conserves energy at coarse resolutions is used for both solid and fluid phases. The δ-correction technique further minimizes quadrature errors from fluid particle clustering. Validated against benchmark cases, including consolidation, dynamic loading, porous dam flow, landslide simulations, and intense bedload by dam-break, our method achieves significant reductions in stress oscillations across both phases while improving fluid particle distribution. This framework delivers a computationally efficient, robust solution for large-deformation solid-fluid coupling in geomechanics, environmental engineering, and beyond.

1. Introduction

Solid-fluid mixtures are ubiquitous in nature and engineering applications, typically comprising porous media interacting with fluids, such as soil-water systems. These mixtures present numerous engineering challenges, ranging from industrial pipeline transportation [1] to the construction of earthen levees and dams [2]. Furthermore, investigating solid-fluid coupling mechanisms enhances our understanding of various geological phenomena, including debris flows [3,4], subaerial and submerged landslides [5,6], and landslide-generated tsunamis [7]. Therefore, research on solid-fluid coupling is essential not only for engineering applications but also for natural disaster mitigation [8–11].

In recent years, numerical algorithms have been extensively developed for simulating solid-fluid coupling problems in porous media. A widely adopted approach employs discrete methods to model the solid phase, such as the Discrete Element Method (DEM) [12–14], combined with various techniques to simulate fluid behavior, including CFD (Computational Fluid Dynamics)-DEM [15–17], LBM (Lattice Boltzmann Method)-DEM [18,19], and SPH (Smoothed Particle Hydrodynamics)-DEM [20,21]. However, these approaches face significant limitations in simulating engineering problems involving large numbers of particles due to prohibitive computational costs [22]. An alternative strategy utilizes continuum-based methods to simulate the solid phase, including the MPM

* Corresponding authors.
E-mail addresses: ceswzhao@ust.hk (S. Zhao), jzhao@ust.hk (J. Zhao).

https://doi.org/10.1016/j.cma.2026.118957
Received 5 January 2026; Received in revised form 5 March 2026; Accepted 28 March 2026
Available online 8 April 2026

[23,24], Finite Element Method (FEM) [25], Particle Finite Element Method (PFEM) [26], SPH [10,27], Peridynamics (PD) [28–30], and Moving Particle Semi-implicit method (MPS) [31]. Among these, MPM is particularly distinguished by its capability to effectively capture Lagrangian flow features through material points while solving motion equations on a temporary Eulerian grid [32–36]. It has demonstrated accuracy and robustness in modeling various solid-like materials subjected to large deformations [22,37,38].

Within the MPM framework, approaches for solid-fluid interaction can be classified into two categories: unified MPM and hybrid methods. The unified MPM describes both solid and fluid phases within a single framework, encompassing techniques such as one-point two-phase [39–42] and two-point two-phase MPM [43–45]. The one-point approach is designed for mixtures where fluid coexists with the solid phase, with pressure carried by solid material points. In contrast, the two-point method employs two distinct sets of material points to independently represent solid and fluid phases, enabling simultaneous simulation of dry granular materials, pure fluids, and their mixtures. Hybrid methods, including MPM-Finite Volume Method (FVM) [22,46], MPM-SPH [47], and MPM-FEM [48,49], have been developed to address complex solid-fluid coupling problems. Among these, the two-point two-phase MPM has been extensively applied to diverse challenges, particularly in simulating extreme large deformations in coastal and geotechnical engineering. MPM's capability to effectively simulate fluid behavior addresses complex physical problems involving moving boundaries and severely deformed interfaces, which pose significant challenges for mesh-based methods [50]. Considering recent advancements in MPM for fluid dynamics simulations [51–56], the continued development of two-point two-phase MPM for solid-fluid coupling problems is both timely and significant.

Volumetric locking represents a significant challenge in explicit MPM simulations, occurring when volumetric constraints exceed the system's degrees of freedom. In explicit MPM, fluids are typically modeled as weakly compressible materials, which restricts volumetric deformation at each fluid material point. This limitation frequently leads to substantial pressure oscillations within the simulated material [57–59]. To address volumetric locking in solid-fluid coupling problems, techniques such as fractional-step [60–63] and monolithic methods [53,64] have been implemented in implicit MPM [40,45,65,66]. However, the convergence of these methods can be adversely affected by nonlinear behavior of local contacts or material responses, potentially limiting their effectiveness in complex scenarios [67,68].

In contrast, explicit MPM formulations are often preferred over implicit schemes due to their simplicity, absence of convergence issues, and capability to leverage GPU parallelism [69,70]. To address volumetric locking in two-phase explicit MPM, various anti-locking techniques have been developed. Bandara and Soga [43] implemented the Selective Reduced Integration (SRI) technique in two-phase MPM to reduce pressure oscillations by replacing pressure at material points with pressure at element centers. Since the SRI technique generates uniform pressure within elements, Zheng et al. [71] employed a Moving Least Squares Approximation (MLSA) to reconstruct the pressure field from central pressure, achieving continuous pressure distribution. Wang et al. [72] adopted cell-averaging for pressure and utilized cubic B-spline basis functions, departing from commonly used GIMP basis functions, enhancing pressure field performance. However, these studies primarily focus on mixtures without considering free water presence. Baumgarten and Kamrin [73] also employed cubic B-spline basis functions to simulate fluid phases under conditions involving free water and mixtures, but achieved limited success in pressure stabilization. Zhang and Liu [74] incorporated the $\bar{F}$ method proposed by Zhao et al. [51] into two-phase MPM, successfully mitigating pressure oscillations in both free water and mixtures. However, they introduced high damping coefficients to reduce solid-fluid coupling effects on the fluid phase, which may lead to inaccuracies in pressure calculations for mixtures under large deformations when relative velocities between solid and fluid phases are significant. Given the current state of two-phase explicit MPM research, there exists a critical need for more robust and accurate stabilization techniques to address mixtures and free water in solid-fluid coupling problems.

While substantial research has focused on addressing pressure fluctuations in MPM, less emphasis has been placed on mitigating stress oscillations in the solid phase. Mast et al. [75] developed a novel approach based on the Hu-Washizu multi-field variational principle, which employs separate approximations for volumetric and deviatoric components of strain and stress fields. This method was effectively applied to dry granular column collapse and reduced stress oscillations in dynamic scenarios [76]. Bandara and Soga [43] introduced the $\bar{B}$ method, which averages strains of material points with those at cell centers, effectively reducing solid stress oscillations in solid-fluid coupling scenarios. Xie et al. [77] utilized mass-weighted deformation gradients to reconstruct strain and achieve smoother stress fields for large-deformation geotechnical modeling. This approach was further extended by Xie et al. [78] to two-phase problems, enhancing solid stress fields in solid-water mixtures. Additionally, Kossler et al. [79] proposed a grid-shifting technique that adjusts the background grid after each time step, to reduce mesh-dependent stress oscillations in pure solid simulations. Despite these advancements, stabilization techniques specifically targeting solid stress oscillations in large-deformation solid-fluid coupling problems remain limited, highlighting the need for further development of stress stabilization methods for the solid phase.

This study presents a stabilized explicit MPM framework for solid-fluid coupling problems, effectively addressing the previously outlined challenges. Building upon an explicit two-point two-phase MPM framework, we implement a dual volume averaging technique utilizing cubic B-spline basis functions to smooth deformation gradients and pressure. This innovative approach significantly mitigates volumetric locking and cell-crossing errors, resulting in more stable and accurate fluid phase simulations. To address stress oscillations in the solid phase during large deformations, we introduce a hybrid smoothing technique that enhances the stress field through cell-based and node-based smoothing for deviatoric and volumetric strain, respectively. Furthermore, the AFLIP scheme is incorporated for both solid and fluid phases to minimize particle-grid mapping errors and ensure energy conservation at relatively coarse grid resolutions. To combat particle clustering, we apply the δ-correction technique to the fluid phase, which reduces quadrature errors and promotes more uniform particle distribution. The efficacy of the proposed MPM framework is demonstrated through several numerical examples covering diverse solid-fluid coupling scenarios.

The remainder of this paper is organized as follows: Section 2 introduces the vanilla two-point two-phase MPM. The enhanced two-point two-phase MPM is proposed in Section 3, where the AFLIP scheme and high-order B-spline basis functions are integrated with stabilization techniques. The proposed framework is verified against a series of benchmark examples in Section 4, followed by a set of numerical examples for complex senarios in Section 5. Finally, Section 6 concludes the paper.

2. Vanilla two-point two-phase MPM

2.1. Governing equations for two-phase porous media

2.1.1. Mass balance equations

In the framework of Lagrangian description, the mass balance equations for solid and fluid phases are expressed as follows [43]:

$$\begin{aligned}\frac{D(m_s)}{Dt} &= \frac{D((1-n)\rho_s V_s)}{Dt} \\ &= \rho_s V_s \frac{\mathrm{D}(1-n)}{Dt} + (1-n)V_s \frac{\mathrm{D}\rho_s}{Dt} + (1-n)\rho_s \frac{\mathrm{D}V_s}{Dt} = 0\end{aligned} \tag{1a}$$

$$\begin{aligned}\frac{D(m_f)}{Dt} &= \frac{D(n\rho_f V_f)}{Dt} \\ &= \rho_f V_f \frac{\mathrm{D}n}{Dt} + nV_f \frac{\mathrm{D}\rho_f}{Dt} + n\rho_f \frac{\mathrm{D}V_f}{Dt} = 0\end{aligned} \tag{1b}$$

where m_α ($\alpha = s$ or f) represents the mass of solid or fluid phases. ρ_α and V_α denote the density and volume, respectively. n is the porosity at the position of material points.

Neglecting density variation of the solid phase, the material time derivative of porosity can be expressed as:

$$\frac{Dn}{Dt} = (1-n)\nabla \cdot \boldsymbol{v}_s. \tag{2}$$

where $\boldsymbol{v}_s$ is the velocity of the solid phase. Substituting Eq. (2) into Eq. (1b) yields

$$\frac{1}{\rho_f}\frac{D\rho_f}{Dt} = -\frac{1}{n}[(1-n)\nabla \cdot \boldsymbol{v}_s + n\nabla \cdot \boldsymbol{v}_f] \tag{3}$$

where $\boldsymbol{v}_f$ is the velocity of the fluid phase. Since the fluid is considered weakly compressible, density variation is related to variation of volumetric strain $\epsilon_{v,f}$ [80], as follows:

$$\frac{D\epsilon_{v,f}}{Dt} = -\frac{1}{\rho_f}\frac{D\rho_f}{Dt} \tag{4}$$

Substituting Eq. (3) into Eq. (4) yields

$$\frac{D\epsilon_{v,f}}{Dt} = \frac{1}{n}\left[(1-n)\nabla \cdot \boldsymbol{v}_s + n\nabla \cdot \boldsymbol{v}_f\right] \tag{5}$$

2.1.2. Momentum balance equations

The momentum equilibrium equations for solid and fluid phases in mixtures are expressed as [43]

$$(1-n)\rho_s \dot{\boldsymbol{v}}_s = \nabla \cdot \boldsymbol{\sigma}'_s - (1-n)\nabla p_f + (1-n)\rho_s \boldsymbol{g} + \boldsymbol{f}_d \tag{6a}$$

$$n\rho_f \dot{\boldsymbol{v}}_f = n\nabla p_f + n\rho_f \boldsymbol{g} - \boldsymbol{f}_d \tag{6b}$$

where $\boldsymbol{\sigma}'_s$ is the stress tensor of the solid phase, p_f is the pressure of the fluid phase (with compression being positive). For pure fluids, Eq. (6b) degenerates to:

$$\rho_f \dot{\boldsymbol{v}}_f = \nabla \cdot \boldsymbol{\sigma}_f + \rho_f \boldsymbol{g} \tag{7}$$

where $\boldsymbol{\sigma}_f$ is the stress tensor of the fluid phase.

The drag force $\boldsymbol{f}_d$ is given by

$$\boldsymbol{f}_d = \frac{n^2 \rho_f g}{k} \cdot (\boldsymbol{v}_f - \boldsymbol{v}_s) + \beta n^3 \rho_f \left|\boldsymbol{v}_f - \boldsymbol{v}_s\right| (\boldsymbol{v}_f - \boldsymbol{v}_s) \tag{8}$$

where k is the Darcy's permeability, β is the non-Darcy flow coefficient, $|\cdot|$ denotes the norm. β is determined following the methodology described by Ergun [81], using the formula $\beta = B/\sqrt{\kappa A n^3}$, where $A = 150$, $B = 1.75$. The Darcy's permeability k can be derived from the intrinsic permeability κ using the following relationship:

$$k = \kappa \frac{\rho_f g}{\mu_f} \tag{9}$$

where μ_f is fluid dynamic viscosity. κ can be calculated using the Kozeny-Carman formula [82,83]:

$$\kappa = \frac{n^3 D_p^2}{150(1-n)^2} \tag{10}$$

where D_p is the particle diameter.

2.2. Constitutive models

2.2.1. Equation of state (EOS) for weakly compressible fluids

The fluid stress can be decomposed into two components:

$$\boldsymbol{\sigma}_f = \boldsymbol{\tau}_f - p_f \mathbf{I} \tag{11}$$

where $\boldsymbol{\tau}_f = 2\mu_f \dot{\boldsymbol{\epsilon}}_{q,f}$ is the deviatoric stress tensor, p_f represents the fluid pressure, and μ_f is the dynamic viscosity. $\mathbf{I}$ is the identity tensor, $\dot{\boldsymbol{\epsilon}}_{q,f}$ is the deviatoric strain rate tensor, with the strain rate $\dot{\boldsymbol{\epsilon}}_f$ defined as:

$$\dot{\boldsymbol{\epsilon}}_f = \frac{1}{2}\left(\nabla \boldsymbol{v}_f + (\nabla \boldsymbol{v}_f)^T\right) \tag{12}$$

The fluid pressure can be explicitly given by the EOS:

$$\frac{Dp_f}{Dt} = -K_f \frac{D\epsilon_{v,f}}{Dt} \tag{13}$$

where K_f is the bulk modulus, $\epsilon_{v,f}$ is the volumetric strain at the fluid phase location. The selection of K_f for water should satisfy the requirement that density fluctuations remain below 3%, as specified by Chen et al. [67]. Under this condition, water can be treated as a weakly compressible fluid. In our numerical examples, we adhere to this criterion when choosing K_f.

2.2.2. Constitutive model for the solid phase

While the introduced framework is general and not restricted to a particular constitutive model for the solid phase, the prevailing Mohr-Coulomb soil model is adopted and employed throughout this work unless stated otherwise. The plastic yield function f for the Mohr-Coulomb model is [24,84]:

$$f = R_{mc} q - p \tan\phi - c \tag{14a}$$

$$R_{mc}(\theta, \phi) = \frac{1}{\sqrt{3}\cos\phi} \sin(\theta + \frac{\pi}{3}) + \frac{1}{3}\cos(\theta + \frac{\pi}{3}) \tan\phi \tag{14b}$$

where p and q are the mean stress and deviatoric stress, respectively. ϕ is the friction angle, c is the cohesion strength, and θ is the Lode angle.

The plastic potential function for the non-associated flow rule is:

$$g^p = \sqrt{(\epsilon c_0 \tan\psi)^2 + (R_{mw} q)^2} - p \tan\psi \tag{15a}$$

$$R_{mw}(\theta, e) = \frac{4(1-e^2)\cos^2\theta + (2e-1)^2}{2(1-e)^2\cos\theta + (2e-1)\sqrt{4(1-e^2)\cos^2\theta + 5e^2 - 4e}} R_{mc}\left(\frac{\pi}{3}, \phi\right) \tag{15b}$$

$$R_{mc}\left(\frac{\pi}{3}, \phi\right) = \frac{3 - \sin\phi}{6\cos\phi} \tag{15c}$$

where c_0 is the initial cohesion yield stress, ϵ and e are parameters for the flow rule curve determination, and ψ denotes the dilatancy angle.

The Rankine tension cutoff is introduced to limit the load-carrying capacity in the tensile region. The corresponding plastic yield function f_t and potential function g_t are given by

$$f_t = p + \frac{2q}{3}\cos\theta - \sigma_t \tag{16a}$$

$$g_t = p + \frac{2q}{3}\cos\theta \tag{16b}$$

where σ_t is the tension strength.

The plastic strain tensor $\boldsymbol{\epsilon}^p$ can be updated as:

$$\frac{D\boldsymbol{\epsilon}^p}{Dt} = \frac{D\lambda}{Dt}\frac{\partial g^p}{\partial \boldsymbol{\sigma}'} \tag{17}$$

where λ is the plastic multiplier. The effective stress $\boldsymbol{\sigma}'$ can be obtained by:

$$\frac{D\boldsymbol{\sigma}'}{Dt} = \mathbf{D}^e : \left(\frac{D\boldsymbol{\epsilon}}{Dt} - \frac{D\boldsymbol{\epsilon}^p}{Dt}\right) \tag{18}$$

where $\mathbf{D}^e$ is the elastic stiffness matrix and $\boldsymbol{\epsilon}$ is the strain tensor.

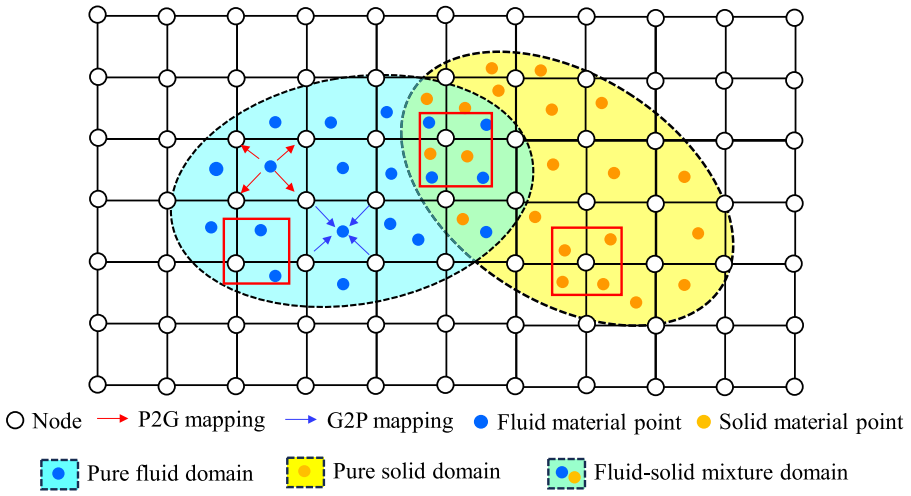

Fig. 1. Illustration of two-point two-phase MPM solution process.

2.3. MPM scheme

2.3.1. Two-point two-phase solution

As illustrated in Fig. 1, the two-point two-phase MPM employs two layers of material points: orange points represent solid material, while blue points represent fluid material. This method builds upon the conventional MPM framework of background grids and material points, thereby enabling the seamless simulation of extreme material deformations. To accurately capture phase interactions, the computational domain is partitioned into three distinct regions based on local mixture conditions: a pure fluid domain, a pure solid domain, and a solid-fluid mixture domain. This explicit regional distinction effectively resolves the ambiguity inherent in mixed-variable representations of single-point methods, allowing for a more physically consistent modeling of key two-phase mechanisms such as relative permeability and fluid seepage through the solid matrix. A two-layer grid framework is adopted, with separate computational grids used to store the nodal information for the solid and fluid phases independently. Interaction forces, including the drag force and fluid pressure, are explicitly coupled between the two phases. The mapping process, which involves both particle-to-grid (P2G) and grid-to-particle (G2P) information transfers, plays a critical role in linking the kinematics of material points with the solutions computed on the background grid. The detailed implementation procedure is summarized below.

2.3.2. P2G mapping

In the P2G mapping process, the mass and momentum of solid and fluid material points are projected onto grid nodes using a basis function:

$$m_{\alpha i}^{k} = \sum_{\alpha p} m_{\alpha p} w_{\alpha i p}^{k} \qquad (\alpha = s, f) \tag{19}$$

$$m_{\alpha i}^{k} \boldsymbol{v}_{\alpha i}^{k} = \sum_{\alpha p} m_{\alpha p} \boldsymbol{v}_{\alpha p}^{k} w_{\alpha i p}^{k} \qquad (\alpha = s, f) \tag{20}$$

where α denotes the phase, i.e., the solid phase s and fluid phase f. The superscript k represents the physical quantity at time step t^k. $m_{\alpha i}^{k}$ represents the nodal mass, mapped from the particle mass $m_{\alpha p}$. $\boldsymbol{v}_{\alpha i}^{k}$ represents the nodal velocity, mapped from the particle velocity $\boldsymbol{v}_{\alpha p}^{k}$. The function $w_{\alpha i p}^{k} = w_{i}^{k}(\boldsymbol{x}_{\alpha p})$ is the interpolation basis function that maps values from node i to the position of material point $\boldsymbol{x}_{\alpha p}$, and $\sum_{\alpha p}$ denotes the summation over all material points affected by the basis function associated with node i. Similarly, the nodal porosity n_i can be mapped from the porosity at the location of solid particles n_{sp} by:

$$m_{si}^{k} n_{i}^{k} = \sum_{sp} m_{sp} n_{sp}^{k} w_{sip}^{k} \tag{21}$$

2.3.3. Solving at nodes

Using the MPM scheme, the momentum balance equations presented in Eq. (6) can be discretized in both spatial and temporal domains as follows:

$$m_{si}^{k} \boldsymbol{a}_{si}^{k+1} = m_{si}^{k} \boldsymbol{g} - \sum_{sp} (\boldsymbol{\sigma'}_{p}^{k} \nabla w_{sip}^{k} V_{sp}^{k}) + (1 - n_{i}^{k}) \sum_{fp} (p_{fp}^{k} \nabla w_{fip}^{k} V_{fp}^{k}) + \boldsymbol{f}_{di}^{k} + \boldsymbol{s}_{si}^{k} \tag{22}$$

$$m_{fi}^{k} \boldsymbol{a}_{fi}^{k+1} = m_{fi}^{k} \boldsymbol{g} - \sum_{fp} (\boldsymbol{\tau}_{fp}^{k} \nabla w_{fp}^{k} V_{fp}^{k}) + n_{i}^{k} \sum_{fp} (p_{fp}^{k} \nabla w_{fip}^{k} V_{fp}^{k}) - \boldsymbol{f}_{d_i}^{k} + \boldsymbol{s}_{fi}^{k} \tag{23}$$

where $\boldsymbol{s}_{si}^{k}$ and $\boldsymbol{s}_{fi}^{k}$ are traction forces imposed on the boundary for solid and fluid phases, respectively. By combining Eqs. (19)–(21) with Eqs. (22)-(23), we can obtain the nodal acceleration $\boldsymbol{a}_{si}^{k+1}$ and $\boldsymbol{a}_{fi}^{k+1}$ for both solid and fluid phases. Then the nodal velocity can be updated as:

$$\boldsymbol{v}_{\alpha i}^{k+1} = \boldsymbol{v}_{\alpha i}^{k} + \boldsymbol{a}_{\alpha i}^{k+1}\Delta t \qquad (\alpha = s, f) \tag{24}$$

2.3.4. G2P mapping

With the solved nodel velocities and accelerations, the information of material points can be updated through the G2P mapping process. To update the velocities of material points, there are two commonly used methods, i.e., the Particle-in-Cell (PIC) method [85] and the Fluid-Implicit Particle (FLIP) method [86], given by

$$\boldsymbol{v}_{\alpha p}^{k+1} = \sum_{i} w_{\alpha i p}\boldsymbol{v}_{\alpha i}^{k+1}, \quad \text{PIC} \qquad (\alpha = s, f) \tag{25a}$$

$$\boldsymbol{v}_{\alpha p}^{k+1} = \boldsymbol{v}_{\alpha p}^{k} + \sum_{i} w_{\alpha i p}\boldsymbol{a}_{\alpha i}^{k+1}\Delta t, \quad \text{FLIP} \qquad (\alpha = s, f) \tag{25b}$$

The particle position $\boldsymbol{x}_{\alpha p}$ can then be updated as:

$$\boldsymbol{x}_{\alpha p}^{k+1} = \boldsymbol{x}_{\alpha p}^{k} + \sum_{i} w_{\alpha i p}\boldsymbol{v}_{\alpha i}^{k+1}\Delta t \qquad (\alpha = s, f) \tag{26}$$

Once the velocity and position of material points are updated, all physical information carried by the background grid is reset. The simulation then advances to the next step, repeating the above procedure.

3. Stabilized two-point two-phase MPM

3.1. AFLIP scheme

Traditional methods, such as PIC [85] and FLIP [86] methods, exhibit unsatisfactory performance in cases involving large deformations. This is primarily due to excessive energy dissipation in PIC and numerical noise inherent in FLIP. The Affine PIC (APIC) method [87] has demonstrated effectiveness in maintaining both energy conservation and numerical stability for large deformation problems in two-phase MPM simulations [45,74]. However, the APIC method requires a sufficiently fine mesh to ensure accurate energy conservation and minimize accuracy loss [88], which significantly increases computational costs in large deformation simulations. A practical and efficient solution is the combination of APIC and FLIP methods (AFLIP) which effectively reduces energy dissipation in single-phase problems even when using relatively coarse meshes [56,89–92]. In this study, the AFLIP mapping scheme is employed for addressing two-phase problems.

At the P2G stage, the APIC scheme introduces a matrix $\boldsymbol{C}_{\alpha p}^{k}$ of different phases $\alpha = s, p$, where the local velocity of a particle at grid node $\boldsymbol{x}_i$ is expressed as $\boldsymbol{v}_{\alpha p}^{k} + \boldsymbol{C}_{\alpha p}^{k}(\boldsymbol{x}_i - \boldsymbol{x}_{\alpha p}^{k})$. This formulation defines the transfer from particles to the grid:

$$m_{\alpha i}^{k}\boldsymbol{v}_{\alpha i}^{k} = \sum_{\alpha p} w_{\alpha i p}^{k} m_{\alpha p}(\boldsymbol{v}_{\alpha p}^{k} + \boldsymbol{C}_{\alpha p}^{k}(\boldsymbol{x}_i - \boldsymbol{x}_{\alpha p}^{k})) \tag{27}$$

where $\boldsymbol{C}_{\alpha p}^{k} = \boldsymbol{B}_{\alpha p}^{k}(\boldsymbol{D}_{\alpha p}^{k})^{-1}$, $\boldsymbol{D}_{\alpha p}^{k}$ is analogous to an inertia matrix for affine motion, given by:

$$\boldsymbol{D}_{\alpha p}^{k} = \sum_{i} w_{\alpha i p}(\boldsymbol{x}_i - \boldsymbol{x}_{\alpha p}^{k})(\boldsymbol{x}_i - \boldsymbol{x}_{\alpha p}^{k})^{\mathrm{T}} \tag{28}$$

$\boldsymbol{B}_{\alpha p}^{k}$ contains angular momentum information and is modified during the process of mapping data from the grid to material points G2P. The corresponding transfer from the grid to material points is expressed as:

$$\boldsymbol{B}_{\alpha p}^{k+1} = \sum_{i} w_{\alpha i p}\boldsymbol{v}_{\alpha i}^{k+1}(\boldsymbol{x}_i - \boldsymbol{x}_{\alpha p}^{k})^{\mathrm{T}} \tag{29}$$

The AFLIP scheme can be expressed as:

$$\boldsymbol{v}_{\alpha p}^{k+1} = (1-\beta)(\boldsymbol{v}_{\alpha p}^{k} + \sum_{i} w_{\alpha i p}\boldsymbol{a}_{\alpha i}^{k+1}\Delta t) + \beta(\sum_{i} w_{\alpha i p}\boldsymbol{v}_{\alpha i}^{k+1}) \tag{30}$$

The blending coefficient $\beta = 1$ corresponds to the APIC scheme, while the FLIP scheme is employed when $\beta = 0$. This coefficient is explicitly defined in each simulation case. If no value is provided, β is assumed to be 1 by default.

3.2. Cubic B-spline basis functions

During the mapping process between material points and grid nodes, basis functions play a crucial role. It has been demonstrated that the accuracy of numerical results obtained using B-spline functions surpasses that of other basis functions [93], such as GIMP [94] and CPDI [95]. For large deformations, cubic B-spline functions offer superior accuracy and stability compared to quadratic B-splines, without significantly increasing computational cost [56]. It has been demonstrated that cubic B-spline functions can substantially mitigate pressure oscillations and permit larger time steps compared to quadratic B-spline functions in fluid simulations, albeit at the cost of increased computational time per step [56]. Therefore, cubic B-spline functions are adopted in this study.

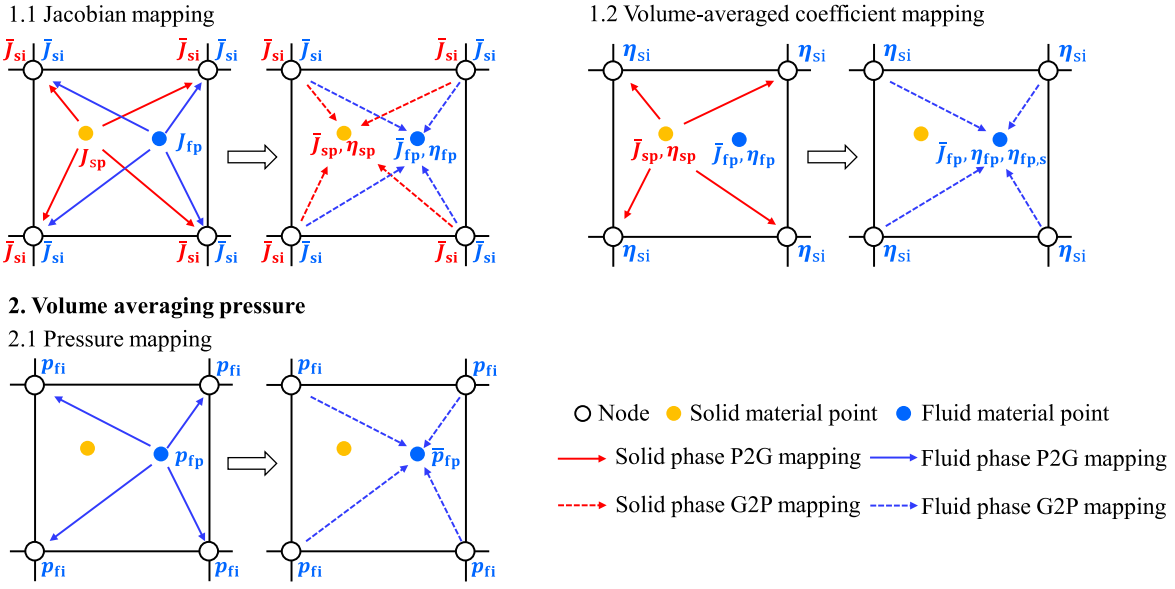

Fig. 2. Schematic diagram of the dual volume averaging process.

The B-spline basis functions can be defined through a knot vector, which is a set of ordered, non-decreasing values in R known as knots. A knot vector is defined by:

$$\Xi = \{\xi_1, \xi_2, \xi_i, \dots, \xi_{n+p+1}\} \tag{31}$$

where ξ_i is the i^{th} knot, i is the knot index, $i = 1, 2, \dots, n + p + 1$.

Let p denote the polynomial degree and n the total number of B-spline basis functions. The knot vector subdivides the parametric domain into different segments or elements. The B-spline basis functions for a given knot vector are constructed step by step using the Cox-de Boor recursion formula [96]:

$$N_{i,p}(\xi) = \frac{\xi - \xi_i}{\xi_{i+p} - \xi_i} N_{i,p-1}(\xi) + \frac{\xi_{i+p+1} - \xi}{\xi_{i+p+1} - \xi_{i+1}} N_{i+1,p-1}(\xi), \quad \text{for } p > 0 \tag{32}$$

with

$$N_{i,0}(\xi) = \begin{cases} 1 & \text{if } \xi_i \leqslant \xi < \xi_{i+1}, \\ 0 & \text{otherwise.} \end{cases} \tag{33}$$

In general, there are four types of cubic B-spline basis functions [97], and their detailed formulations can be found in Cheng et al. [56], Vaucorbeil et al. [97].

3.3. Stabilization techniques

3.3.1. Fluid phase: Dual volume averaging

We introduce a dual volume averaging technique to mitigate pressure oscillations in the fluid phase, i.e., volume averaging both deformation and pressure. As illustrated in Fig. 2, the first volume averaging step, involving deformation gradients, consists of two sub-steps: mapping of Jacobian $J_{\alpha p}$ and mapping of the volume-averaged coefficient $\eta_{\alpha p}$. The term $J_{\alpha p}$, defined as the determinant of the deformation gradient at the particle location, is first mapped to nodes to obtain nodal Jacobian $\bar{J}_{\alpha i}$. These nodal values are then mapped back to particles to yield the volume-averaged Jacobian $\bar{J}_{\alpha p}$, from which $\eta_{\alpha p}$ is computed. To determine the solid volume-averaged coefficient at fluid particle positions, $\eta_{fp,s}$, a double mapping of η_{sp} is performed. The coefficients $\eta_{fp,s}$ and η_{fp} are subsequently used to compute volume-averaged deformation gradients for fluid strain and pressure. In the second volume averaging step, a similar mapping procedure is applied to fluid pressure p_{fp} to obtain the volume-averaged pressure $\bar{p}_{fp}$. This averaged pressure is then substituted into Eqs. (22)-(23) to solve the momentum equilibrium equations.

The key idea of the first volume averaging is to replace original deformation gradients with assumed deformation gradients [51], using:

$$\bar{\boldsymbol{F}}_p^{k+1} = \left(\frac{\bar{J}_p^{k+1}}{J_p^{k+1}} \right)^{1/\dim} \boldsymbol{F}_p^{k+1} \tag{34}$$

where $\boldsymbol{F}_p^{k+1}$ and $\bar{\boldsymbol{F}}_p^{k+1}$ are the original and assumed deformation gradient at t^{k+1}, respectively. $J_p^{k+1} = \det \boldsymbol{F}_p^{k+1}$ is the determinant of the deformation gradient at t^{k+1} and dim is the simulation dimension that is set to 2 and 3 for 2D and 3D cases, respectively.

In explicit time integration schemes, where stresses accumulate over successive time steps, it is necessary to introduce an assumed relative deformation gradient $\Delta\bar{\boldsymbol{F}}_p^{k+1}$. The following equations describe the relationships between the various deformation measures at the material point:

$$\bar{\boldsymbol{F}}_p^{k+1} = \Delta\bar{\boldsymbol{F}}_p^{k+1} \cdot \bar{\boldsymbol{F}}_p^{k} \tag{35a}$$

$$\boldsymbol{F}_p^{k+1} = \Delta\boldsymbol{F}_p^{k+1} \cdot \boldsymbol{F}_p^{k} \tag{35b}$$

$$J_p^{k+1} = \Delta J_p^{k+1} J_p^{k} \tag{35c}$$

$$\bar{\boldsymbol{F}}_p^{k} = \left(\frac{\bar{J}_p^{k}}{J_p^{k}}\right)^{1/\dim} \boldsymbol{F}_p^{k} \tag{35d}$$

where $\Delta J_p^{k+1} = \det \Delta\boldsymbol{F}_p^{k+1}$ represents the determinant of the relative deformation gradient at t^{k+1}. In this context, substituting Eq. (35) into Eq. (34), the deformation gradient can be replaced by its relative form, yielding [51]:

$$\Delta\bar{\boldsymbol{F}}_p^{k+1} = \left(\frac{\bar{J}_p^{k+1}}{\bar{J}_p^{k}\Delta J_p^{k+1}}\right)^{1/\dim} \Delta\boldsymbol{F}_p^{k+1} \tag{36}$$

For the fluid pressure of mixtures, we can obtain the formula with Eqs. (5) and (13):

$$\frac{Dp_f}{Dt} = -\frac{K_f}{n}\left[(1-n)\nabla\cdot\boldsymbol{v}_s + n\nabla\cdot\boldsymbol{v}_f\right] \tag{37}$$

The pressure in the fluid phase is determined based on volumetric strains of both fluid and solid phases at the fluid material point location. The volumetric strain of the solid phase at fluid particles is obtained by interpolating the surrounding solid phase strain field. Therefore, to compute the pressure of mixtures, it is necessary to evaluate the volume-averaged relative deformation gradients $\Delta\bar{\boldsymbol{F}}_p$ for both phases. The implementation details are described below.

The original relative deformation gradient of different phases $\alpha = s, p$ at t^{k+1} is calculated by:

$$\Delta\boldsymbol{F}_{\alpha p}^{k+1} = 1 + \Delta t \sum_i \boldsymbol{v}_{\alpha i}^{k+1} \otimes \nabla w_{i\alpha p} \tag{38}$$

The volume of material points $V_{\alpha p}$ can be updated as:

$$V_{\alpha p}^{k+1} = \boldsymbol{J}_{\alpha p}^{k+1} \cdot V_{\alpha p}^{0} \tag{39}$$

where $J_{\alpha p}^{k+1} = \det \boldsymbol{F}_{\alpha p}^{k+1}$ is the determinant of deformation gradients at t^{k+1}. The nodal volume-averaged Jacobian are given by:

$$\bar{J}_{\alpha i}^{k+1} = \sum_{\alpha p} w_{i\alpha p} V_{\alpha p}^{k} (\bar{J}_{\alpha p}^{k} \Delta J_{\alpha p}^{k+1}) / V_{\alpha i}^{k} \tag{40}$$

with

$$V_{\alpha i}^{k} = \sum_{\alpha p} w_{i\alpha p} V_{\alpha p}^{k} \tag{41a}$$

$$\Delta J_{\alpha p}^{k+1} = \det(\Delta\boldsymbol{F}_{\alpha p}^{k+1}) \tag{41b}$$

$$\bar{J}_{\alpha p}^{k} = \det(\bar{\boldsymbol{F}}_{\alpha p}^{k}) \tag{41c}$$

Then mapping the nodal volume-averaged Jacobian to particles yields:

$$\bar{J}_{\alpha p}^{k+1} = \sum_i w_{i\alpha p} \bar{J}_{\alpha i}^{k+1} \tag{42}$$

According to Eq. (36), the relative assumed deformation gradient $\Delta\bar{\boldsymbol{F}}_p^{k+1}$ can be obtained by the volume-averaged coefficient $\eta_{\alpha p}^{k+1}$ at t^{k+1}, given by:

$$\eta_{\alpha p}^{k+1} = \left(\frac{\bar{J}_{\alpha p}^{k+1}}{\bar{J}_{\alpha p}^{k}\Delta J_{\alpha p}^{k+1}}\right)^{1/\dim} \tag{43}$$

The assumed relative fluid deformation gradients at the position of fluid material points $\Delta\bar{\boldsymbol{F}}_{fp}^{k+1}$ is calculated by:

$$\Delta\bar{\boldsymbol{F}}_{fp}^{k+1} = \eta_{fp}^{k+1}\Delta\boldsymbol{F}_{fp}^{k+1} \tag{44}$$

To obtain the assumed relative solid deformation gradients at fluid material points, the solid volume-averaged coefficient at solid material points must first be mapped to the nodes:

$$\eta_{si}^{k+1} = \sum_{sp} w_{isp} m_{sp} \eta_{sp}^{k+1} / m_{si}^{k+1} \tag{45}$$

Then interpolate it to the position of fluid material points, the solid volume-averaged coefficient at the position of fluid material points $\eta_{fp,s}^{k+1}$ is given by:

$$\eta_{fp,s}^{k+1} = \sum_i w_{ifp}\eta_{si}^{k+1} \tag{46}$$

Similarly, the assumed relative solid deformation gradients at the position of fluid material points $\Delta\bar{\boldsymbol{F}}_{fp,s}^{k+1}$ is calculated by:

$$\Delta\bar{\boldsymbol{F}}_{fp,s}^{k+1} = \eta_{fp,s}^{k+1}\Delta\boldsymbol{F}_{fp,s}^{k+1} \tag{47}$$

where the original relative solid deformation gradients at the position of fluid material points $\Delta\boldsymbol{F}_{fp,s}^{k+1}$ is given by:

$$\Delta\boldsymbol{F}_{fp,s}^{k+1} = 1 + \Delta t\sum_i \boldsymbol{v}_{si}^{k+1}\otimes\nabla w_{ifp} \tag{48}$$

Therefore, the pressure of the fluid phase can be computed using the EOS presented in Eq. (37), based on the $\Delta\bar{\boldsymbol{F}}_{fp}^{n+1}$ and $\Delta\bar{\boldsymbol{F}}_{fp,s}^{n+1}$ at the position of fluid material points. Additionally, the shear stress, as described in Eq. (11), can also be calculated. Next, update $\bar{\boldsymbol{F}}_{\alpha p}^{k+1} = \Delta\bar{\boldsymbol{F}}_{\alpha p}^{k+1}\cdot\bar{\boldsymbol{F}}_{\alpha p}^{k}$, as the nodal volume-averaged Jacobian given by Eq. (40) for the subsequent step must be calculated using the determinant of $\bar{\boldsymbol{F}}_{\alpha p}^{k+1}$.

We assume that volumetric strain and pressure are continuous across the soil-water interface, while only the porosity differs between the mixture and free water. For pore water within the mixture, porosity is interpolated from the solid material points, whereas for free water, the porosity is set to 1.0. In the volume averaging procedure applied to water material points, free water and pore water are treated as a continuous medium. Consequently, the volumetric strain at the interface is influenced by both free water and pore water. Using the porosity and volume-averaged strain, the pressure for water material points at the interface can then be computed using Eq. (37).

After obtaining the pressure of the fluid phase, the π projection technique is then applied [56,98] as follows:

$$\pi(\bar{p}_{fp})_i^{k+1} = \sum_{fp} w_{ifp}V_{fp}^k {p_{fp}}^{k+1}/V_{fi}^k \tag{49a}$$

$$V_{fi}^k = \sum_{fp} w_{ifp}V_{fp}^k \tag{49b}$$

so that the volume-averaged pressure reads:

$$\bar{p}_{fp}^{k+1} = \sum_i w_{ifp}\pi(\bar{p}_{fp})_i^{k+1} \tag{50}$$

The volume-averaged pressure $\bar{p}_{fp}^{k+1}$ is employed in Eqs. (22) and (23) to solve the momentum equation and update the nodal velocity. The sequential application of volume averaging to both the deformation gradient and the pressure thereby significantly alleviates volumetric locking in large-deformation problems. Although dual volume averaging inherently introduces numerical dissipation, it can be managed through increased time steps as demonstrated in Cheng et al. [56]. In practice, applying pressure volume averaging at predefined intervals rather than at each time step, can also provides an effective strategy to balance numerical stability and dissipation control.

3.3.2. Fluid phase: δ-correction

The MPM is susceptible to accumulating integration errors due to particle clustering in pure fluids or mixtures with low solid volume fractions [22]. To mitigate these errors in fluid simulations, the particle shifting technique (PST) has attracted increasing interest. Various PST approaches have been developed, including the Avoid-a-Void method [99], SPH-inspired shifting techniques [100,101], and the δ-correction scheme [53,59]. Among these, the δ-correction method performs particle shifting using the background grid based on nodal integration errors, eliminating the need for neighbor search and thus reducing computational overhead compared to other PST variants [59,102]. While this approach has been effectively applied in single-phase fluid simulations [53,56,59], its performance in two-phase systems has not yet been investigated. In this work, we implement the δ-correction technique in coupled solid-fluid simulations, with detailed implementation steps provided in Baumgarten et al. [22], Cheng et al. [56].

3.3.3. Solid phase: Hybrid strain smoothing

The solid phase is typically modeled as a continuum capable of undergoing free deformations in both volumetric and deviatoric modes. Consequently, previous anti-locking algorithms developed for the fluid phase to overcome volumetric locking frequently demonstrate limited efficacy when implemented for solid-phase simulations. In this subsection, a new strain smoothing method is proposed for the solid phase to reduce stress oscillations in large-deformation problems. As shown in Fig. 3, the key idea is to perform a double mapping of volumetric strain to obtain volume-averaged values, while replacing deviatoric strain with the value at the cell center. The reconstructed strain field will then be used for stress calculations. The detailed process is described below.

The strain rate for the solid phase can be decoupled into deviatoric and volumetric parts, expressed as:

$$\dot{\boldsymbol{\epsilon}}_s = \dot{\boldsymbol{\epsilon}}_{d,s} + \dot{\epsilon}_{v,s}\mathbf{I} \tag{51}$$

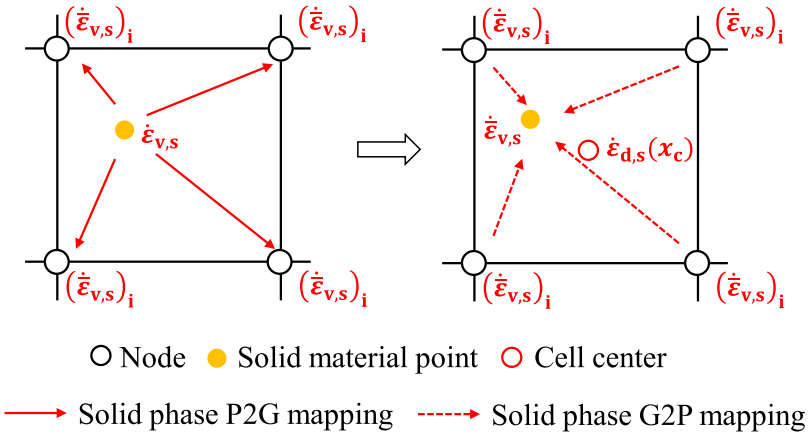

Fig. 3. Schematic diagram of the hybrid smoothing procedure.

where $\dot{\epsilon}_s = \frac{1}{2}\left(\nabla \boldsymbol{v}_s + (\nabla \boldsymbol{v}_s)^T\right)$, $\dot{\epsilon}_{v,s} = \frac{1}{3}(\nabla \cdot \boldsymbol{v}_s)$. After obtaining the volumetric strain $\dot{\epsilon}_{v,s}$ of the solid phase, the π projection technique is then applied [98] as follows:

$$\pi(\dot{\bar{\epsilon}}_{v,s})_i^{k+1} = \sum_{sp} w_{isp} V_{sp}^k \dot{\epsilon}_{v,s}^{k+1} / V_{si}^k \tag{52a}$$

$$V_{si}^k = \sum_{sp} w_{isp} V_{sp}^k \tag{52b}$$

where V_{sp} is the volume of the solid phase. Similarly, the volume-averaged volumetric strain $\dot{\bar{\epsilon}}_{v,s}^{k+1}$ reads:

$$\dot{\bar{\epsilon}}_{v,s}^{k+1} = \sum_i w_{isp} \pi(\dot{\bar{\epsilon}}_{v,s})_i^{k+1} \tag{53}$$

The double mapping process serves as a filter for volumetric strain, effectively attenuating high-frequency strain fluctuations while preserving low-frequency components. This filtering mechanism contributes to a smoother volumetric strain field for stabilized pressure computation. To calculate the deviatoric strain $\dot{\boldsymbol{\epsilon}}_{d,s}$, we employ the SRI technique by replacing the original deviatoric strain with its cell-centered counterpart $\dot{\boldsymbol{\epsilon}}_{d,s}(\boldsymbol{x}_c)$. This is achieved by interpolating the nodal velocity at the cell center. Unlike volumetric strain, the deviatoric strain field tends to localize, often manifesting as shear bands, which are high-frequency components. The mapping procedure may filter out these important high-frequency components, potentially compromising the accuracy of deviatoric strain representation. Therefore, the cell-center value selected for $\dot{\boldsymbol{\epsilon}}_{d,s}$ is employed as an optimal compromise between oscillation reduction and accuracy preservation. Thus the new hybrid strain $\dot{\bar{\boldsymbol{\epsilon}}}_s$ can be expressed as:

$$\dot{\bar{\boldsymbol{\epsilon}}}_s = \dot{\boldsymbol{\epsilon}}_{d,s}(\boldsymbol{x}_c) + \dot{\bar{\epsilon}}_{v,s}\mathbf{I} \tag{54}$$

This strain will be input into the constitutive model for stress calculations.

3.4. Critical time step criterion

The explicit MPM uses the central difference method for time integration, which is conditionally stable. To ensure numerical stability, the time step Δt must remain below a critical threshold Δt_c. This criterion, known as the Courant-Friedrichs-Lewy (CFL) condition [43,103], is expressed as:

$$\Delta t_c = \min \frac{h^e}{c_p} \tag{55}$$

where h^e is the characteristic length of the element, c_p is the pressure wave velocity of the soil-water mixture which is defined as:

$$c_p = \sqrt{\frac{\left(\frac{n}{K_f} + \frac{1-n}{K_s}\right)^{-1} + \frac{4}{3}G}{(1-n)\rho_s + n\rho_w}} \tag{56}$$

where K_f is the bulk modulus of fluids, K_s is the bulk modulus of solid grains, and G is the shear modulus of solid skeleton.

3.5. Computational workflow

The overall computational workflow for the proposed explicit stabilized framework is detailed in Algorithm 1. In addition to the stabilization techniques discussed above, two boundary handling methods are adopted: one for the free surface and another for nonrigid-rigid boundaries.

Algorithm 1: Pseudocode of explicit two-point two-phase MPM with the proposed stabilized algorithm.

initialize model;
  Set up particle data: $\boldsymbol{x}_{\alpha p}$, $m_{\alpha p}$, $\boldsymbol{v}_{\alpha p}$, etc.;
  Set up material parameters: E_s, ν_s, K_f, μ_f, etc.;

Input: Simulation time-steps;
foreach *timestep* **do**
  Reset dynamics and P2G mapping:
    Reset nodal dynamics $m_{\alpha i}$, $\boldsymbol{v}_{\alpha i}$, $\boldsymbol{a}_{\alpha i}$ and initialize basis functions $w_{\alpha i p}$.
    Map particle' mass $m_{\alpha p}$, momentum $m_{\alpha p}\boldsymbol{v}_{\alpha p}$ and porosity $m_{sp}n_{sp}$ to nodes.
  Boundary Handling:
    Apply Dirichlet or Neumann boundary conditions.
    Detect free-surface nodes, set $p_{fi} = 0$.
    Apply DEM contact forces for nonrigid-rigid contact boundaries.
  Dual volume averaging for the fluid phase:
    Calculate volume-averaged $\Delta\bar{\boldsymbol{F}}_{fp}$ using Eq. (44) and $\Delta\bar{\boldsymbol{F}}_{fp,s}$ using Eq. (47)
    Compute strain rate $\dot{\boldsymbol{\epsilon}}_f$ using Eq. (12) and stress $\boldsymbol{\sigma}_f$ using Eq. (11).
    Calculate volume-averaged pressure $\bar{p}_{fp}$ using Eq. (50).
  Hybrid strain smoothing for the solid phase:
    Calculate the volume-averaged $\dot{\bar{\epsilon}}_{v,s}$ using Eq. (53) and cell center $\dot{\bar{\boldsymbol{\epsilon}}}_{d,s}(\boldsymbol{x}_c)$.
    Construct the hybrid strain rate $\dot{\bar{\boldsymbol{\epsilon}}}_s$ using Eq. (54) for stress.
  Solution of Variables:
    Map particle's forces to nodes and update nodal information $\boldsymbol{v}_{\alpha i}$, $\boldsymbol{a}_{\alpha i}$.
    Map nodal information to particles, update $\boldsymbol{v}_{\alpha p}$ and $\boldsymbol{x}_{\alpha p}$ using the AFLIP scheme.
  Particle shifting for the fluid phase:
    Apply δ-correction and relocate fluid material points $\boldsymbol{x}'_{fp}$.

In large-deformation solid-fluid coupling simulations, free water typically undergoes significant deformations and maintains non-zero pressure near free surfaces. This behavior conflicts with the zero Dirichlet pressure boundary condition typically applied to free surfaces in pure fluid simulations. To resolve this discrepancy, we employ a simple free surface tracking method developed by Kularathna [104]. Additionally, to model interactions between rigid boundaries and solid/fluid material points, we implement a DEM-enriched contact algorithm [24] capable of handling complex geometries. This approach computes contact forces based on the overlap between material points and rigid blocks using DEM, and then applies these forces to the corresponding material points. The complete implementation procedure is described in Chen et al. [24], Cheng et al. [56].

4. Verification and benchmark

4.1. 1D consolidation test

Terzaghi's 1D consolidation theory [105] is employed to benchmark the coupled framework. The theory applies to isotropic, homogeneous, fully saturated elastic materials under small strain conditions.

The 1D consolidation test was simulated using coupled MPM for plane strain conditions (see Fig. 4(a)). The model consists of a 1.0 m height × 0.02 m wide saturated soil column, discretized with 200 soil material points and 200 water material points. The background grid uses square cells with $L = 0.02$ m containing 4 material points per cell. The solid phase follows an isotropic linear elastic model, while the water phase is modeled as weakly compressible. Material parameters are: solid grain density $\rho_s = 2650$ kg/m^3, Young's modulus $E_s = 10$ MPa, Poisson's ratio $\nu = 0.3$, water density $\rho_w = 1000$ kg/m^3, bulk modulus $K_w = 2.2$ GPa, and dynamic viscosity $\mu_w = 0.001$ Pa·s. Initial conditions specify zero pore pressure and effective stresses, with porosity $n_0 = 0.3$ and Darcy's permeability $k_0 = 1 \times 10^{-3}$ m/s.

A 10 kPa traction p_0 is applied at the drained top surface, with boundary conditions including horizontal constraints on both sides, and full fixation at the base. The simulation uses a time step $\Delta t = 1 \times 10^{-5}$ s. Fig. 4(b) compares numerical results with the analytical solution through normalized pore pressure p/p_0 versus normalized height h/H at different normalized times $T_v = c_v t/H^2$. The close agreement confirms the accuracy of the two-phase MPM implementation.

4.2. 2D Cryer's problem

The Mandel-Cryer effect describes the characteristic non-monotonic pore pressure evolution that can only be properly captured through coupled formulations such as 2D Biot's theory, unlike uncoupled approaches like Terzaghi's 1D consolidation theory [106–108]. Cryer [107] originally developed this theory for an isotropic poroelastic sphere subjected to hydrostatic loading, demonstrating

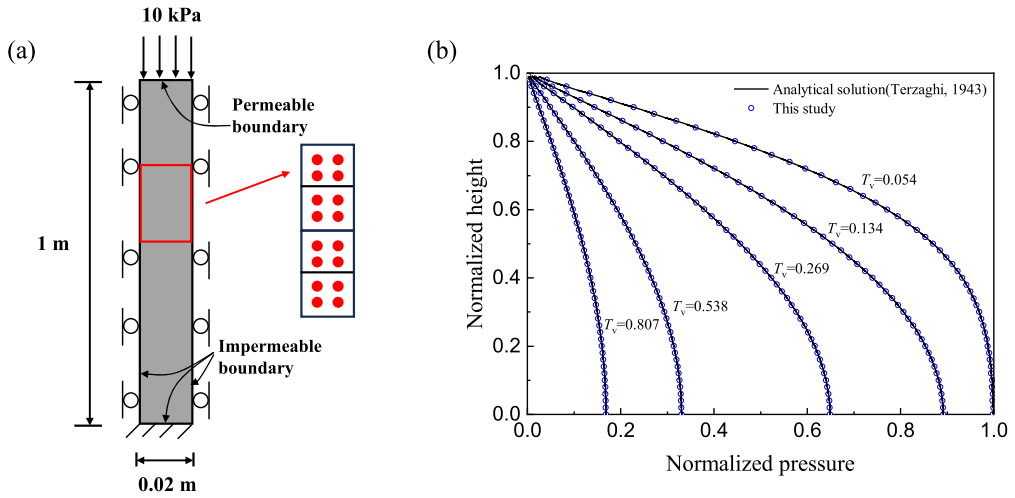

Fig. 4. 1D consolidation: (a) initial configuration and boundary conditions; (b) comparison of pore pressure variation with analytical solution.

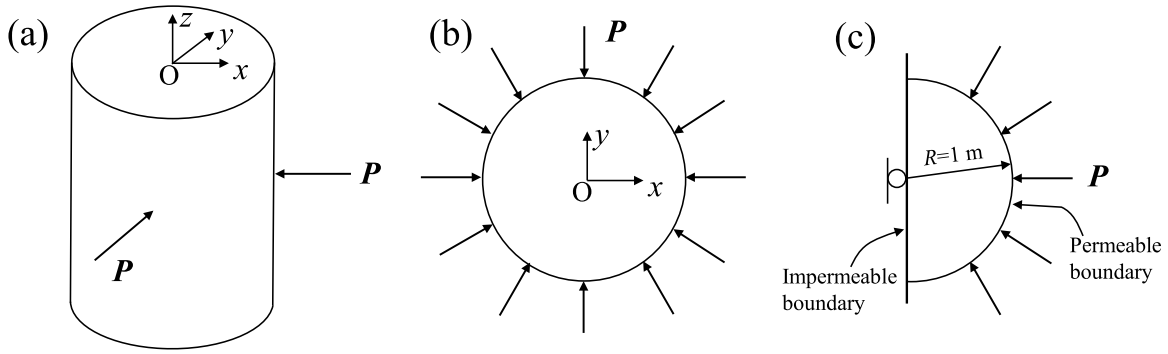

Fig. 5. 2D Cryer's Problem: (a) the original 3D model; (b) an equivalent 2D plane strain model; (c) a half-domain model considering symmetry.

that the generated pore pressure at the specimen's center may surpass the externally applied pressure in saturated media. To validate the coupled MPM formulation, the present study employs the classical Cryer's cylinder problem as a benchmark case (see Fig. 5(a)).

The numerical model employs a 2D plane strain representation of the cylinder, as depicted in Fig. 5(b). Exploiting symmetry, only half of the domain is simulated in Fig. 5(c). Initial conditions specify zero pore pressure throughout the domain, with application of 10 kPa normal traction P on the semicircular surface while permitting drainage at the outer boundary. The symmetry line maintains an impermeable boundary condition. Four distinct cases are examined with Poisson's ratios ν of 0.1, 0.2, 0.3, and 0.4, neglecting gravitational effects. The model configuration features radius $R = 1$ m, discretized with elements of 0.02 m size containing 4 particles each, yielding totals of 15,714 solid and 15,714 water material points. The solid phase follows an isotropic linear elastic constitutive model with material properties: solid grain density $\rho_s = 3000\,\mathrm{kg/m^3}$, Young's modulus $E_s = 10$ MPa. The water phase is characterized by density $\rho_w = 1000\,\mathrm{kg/m^3}$, bulk modulus $K_w = 2.2$ GPa, and dynamic viscosity $\mu_w = 0.001$ Pa·s. Initial conditions include porosity $n_0 = 0.3$ and permeability $k_0 = 1 \times 10^{-3}$ m/s.

Fig. 6(a) displays the pore pressure distribution within the model at different time instants for $\nu = 0.3$, revealing a smooth pressure field that validates the effectiveness of the proposed stabilization method. The temporal evolution of pressure and radial stress at the circle's center are presented in Fig. 6(b) and (c), respectively. Normalized variables, including normalized time $T_v = c_v t/R^2$, normalized pressure p/p_0 (p_0 is the initial pressure after applying the traction), and normalized radial stress σ_r/P, are utilized for the plots. Fig. 6(b) demonstrates the characteristic Mandel-Cryer effect, with the central pressure initially peaking before gradually dissipating to zero. Correspondingly, Fig. 6(c) illustrates the radial stress evolution, which monotonically increases toward the applied traction magnitude P. The numerical solutions are further validated against the 2D Cryer's analytical solution for various Poisson's ratios ν [108–110]. The close agreement between numerical and analytical results for both pressure and stress fields confirms the accuracy and robustness of the stabilized computational framework.

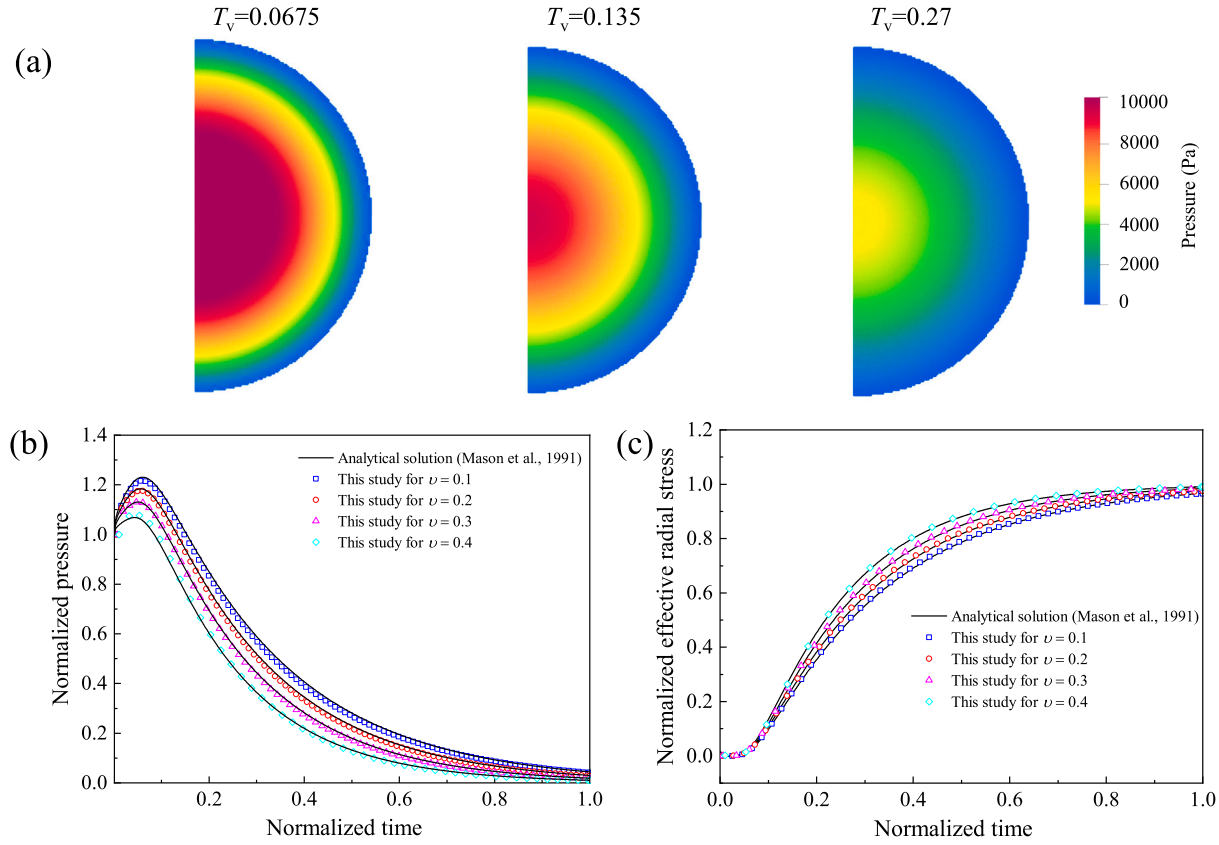

Fig. 6. 2D Cryer's problem: (a) pressure contours of $\nu = 0.3$ at different time; (b) pore pressure variation at the center with different ν; (c) radial stress at the center with different ν.

4.3. Submerged consolidation under gravity

This benchmark study examines the mechanical response of a fully saturated, homogeneous soil column under gravitational loading. The numerical implementation is verified by comparing the simulated hydrostatic pressure and soil stress distribution against analytical solutions.

The computational domain, illustrated in Fig. 7(a), measures 10 m in width and 12 m in height, completely filled with water above a 10 m thick saturated soil layer. Following established methodologies [6,45], the solid phase is characterized as an isotropic linear elastic material with the following properties: solid grain density $\rho_s = 2650\,\mathrm{kg/m^3}$, Young's modulus $E_s = 5\,\mathrm{MPa}$, and Poisson's ratio $\nu = 0.3$. The water phase is defined by density $\rho_w = 1000\,\mathrm{kg/m^3}$, bulk modulus $K_w = 20\,\mathrm{MPa}$, and dynamic viscosity $\mu_w = 0.001\,\mathrm{Pa{\cdot}s}$. The porous medium has initial porosity $n_0 = 0.4$ and permeability $k_0 = 0.4$ m/s.

The boundary conditions are specified as follows: full fixation in vertical and horizontal motions of the bottom boundary, horizontal constraint along the lateral boundaries, and the drainage boundary on the upper surface. A gravitational acceleration $g = 9.81\,\mathrm{m/s^2}$ acts uniformly on both phases. The computational domain employs a uniform discretization of 0.25 m element size, with four solid and four water material points per element, totaling 7680 water material points and 6400 solid material points.

The numerical simulation spans 5.0 s with a constant time step of 1×10^{-5} s. Initial conditions assume zero stress states for both phases, with gravity applied instantaneously at $t = 0$ s and maintained constant. Fig. 7(b) and (c) display the equilibrium distributions of pore water pressure and vertical effective stress, revealing smooth stress fields that demonstrate the ability to reduce oscillations of the stabilized explicit MPM formulation. Quantitative comparison with analytical solutions in Fig. 8 shows excellent agreement for both water pressure and vertical stress profiles. This correspondence validates the framework's capability to accurately predict initial in-situ stresses and pore pressure distributions, confirming proper implementation of the coupled MPM methodology.

4.4. Single-phase dynamic problems

Previous verification studies have predominantly examined static problems, yielding satisfactory results regarding both accuracy and stability. Dynamic problems, however, present greater challenges for numerical simulations due to larger deformations and more complex physical processes. To systematically evaluate the proposed stabilized MPM framework, this study initiates dynamic verification with fundamental single-phase problems: a dam break scenario for fluid dynamics and a column collapse for solid mechanics.

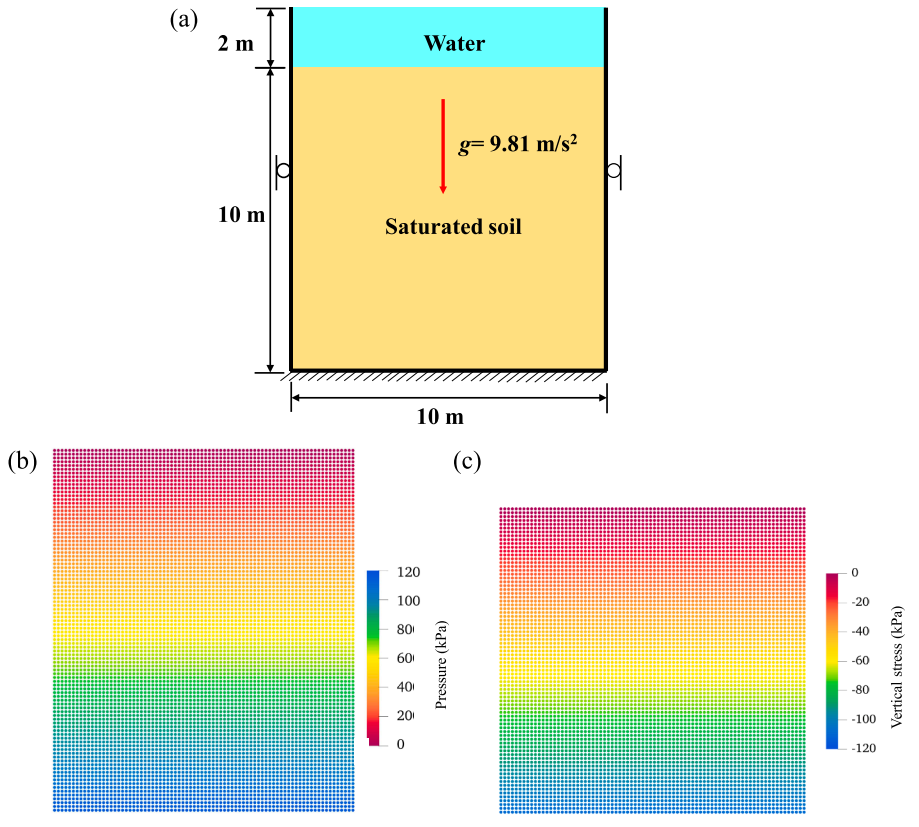

Fig. 7. Submerged consolidation: (a) initial configuration and boundary conditions; (b) water pressure at stable time; (c) vertical stress σ_{yy} (with compression being negative) in the soil skeleton at a stable time.

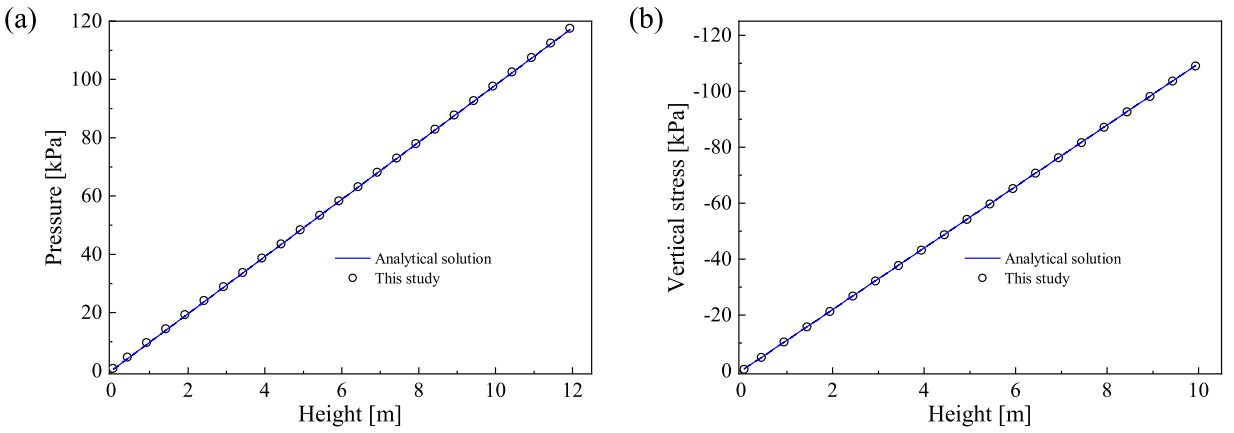

Fig. 8. Submerged consolidation: comparison of (a) pore pressure and (b) vertical stress with analytical solution.

4.4.1. Dam break

Fig. 9 presents the computational domain geometry and boundary conditions. The initial configuration consists of a 0.2 m high × 0.1 m long water column retained by a temporary gate for consolidation purposes, with slip wall conditions applied to all surrounding boundaries. Following gravitational settling and equilibrium establishment, the gate is instantaneously removed to initiate free-surface flow under gravity.

The simulation parameters include: density $\rho = 1000\,\mathrm{kg/m^3}$, bulk modulus $K = 10\,\mathrm{MPa}$, dynamic viscosity $\mu = 0.001\,\mathrm{Pa \cdot s}$, and gravitational acceleration $g = 9.81\,\mathrm{m/s^2}$. Spatial discretization employs a uniform square grid with element size $h = 0.0025\,\mathrm{m}$ with 2 × 2 particle initialization per fluid cell, yielding 12,800 material points. The temporal resolution uses a fixed time step $\Delta t = 1 \times 10^{-5}\,\mathrm{s}$.

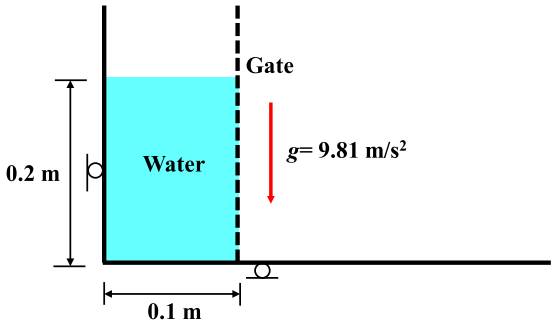

Fig. 9. Dam break: initial configuration and boundary conditions.

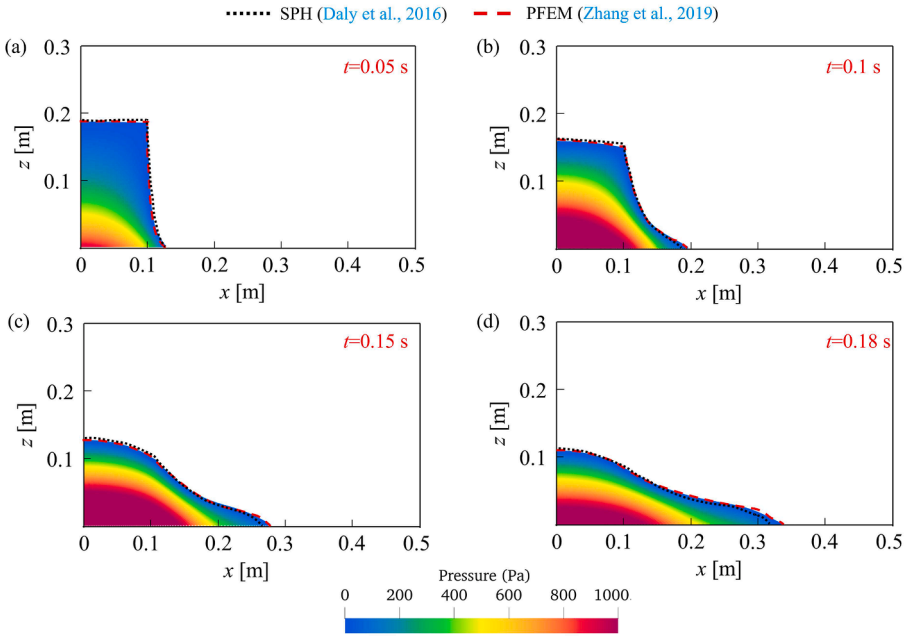

Fig. 10. Comparison of water configuration with previous studies: (a) $t = 0.05$ s; (b) $t = 0.1$ s; (c) $t = 0.15$ s; (d) $t = 0.18$ s.

Fig. 10 displays four sequential snapshots of dam break evolution with corresponding pressure fields. Comparative results from SPH [111] and PFEM [112] implementations demonstrate excellent agreement. The smooth pressure contours and absence of volumetric locking artifacts validate the fluid solver's robustness and numerical stability.

4.4.2. Column collapse

This single-phase solid mechanics benchmark replicates the granular column collapse experiment documented in Lajeunesse et al. [113], providing a direct counterpart to the fluid dam-break problem. The experimental configuration in Fig. 11 features a granular column measuring 0.056 m in width $\times$ 0.1344 m in height. The numerical simulation employs a Mohr-Coulomb constitutive model with material parameters matching the experimental characterization [113]: density $\rho_s = 2500\,\mathrm{kg/m^3}$, Young's modulus $E_s = 1$ MPa, Poisson's ratio $\nu = 0.3$, and friction angle $\phi = 28°$. The model assumes zero cohesion $c = 0$ and zero dilation angle $\psi = 0$.

The computational domain utilizes a uniform square grid $h = 0.002$ m with 2×2 particle initialization per cell, discretizing the solid domain into 7504 material points. The analysis adopts a time step of $\Delta t = 5 \times 10^{-6}$ s with gravitational acceleration $g = 9.81\,\mathrm{m/s^2}$. A temporary retaining gate maintains initial static equilibrium, with boundary conditions including: slip condition on the left boundary, and rough basal surface with friction coefficient $\mu = 0.53$ (derived from $\tan\phi$). Following gravitational settling, gate removal triggers dynamic collapse under gravity.

Fig. 12 compares the vertical stress distribution at equilibrium state with experimental measurements. Both Fig. 12(a) and (b) demonstrate excellent agreement with the experimental final configuration, denoted by the blue dashed line, validating the effectiveness of the hybrid strain smoothing technique. The proposed methodology substantially reduces stress oscillations, particularly near boundary regions, effectively mitigating locking phenomena in dynamic simulations.

Fig. 13 displays four sequential stages of column collapse with corresponding vertical stress distributions. The numerical simulation exhibits faster collapse progression compared to experimental observations, primarily due to the idealized instantaneous gate removal

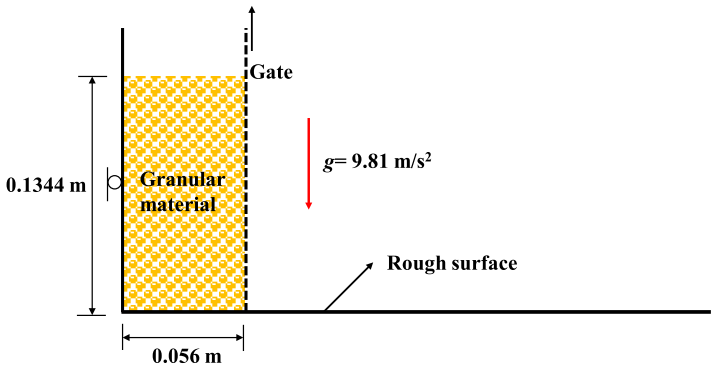

Fig. 11. Column collapse: initial configuration and boundary conditions.

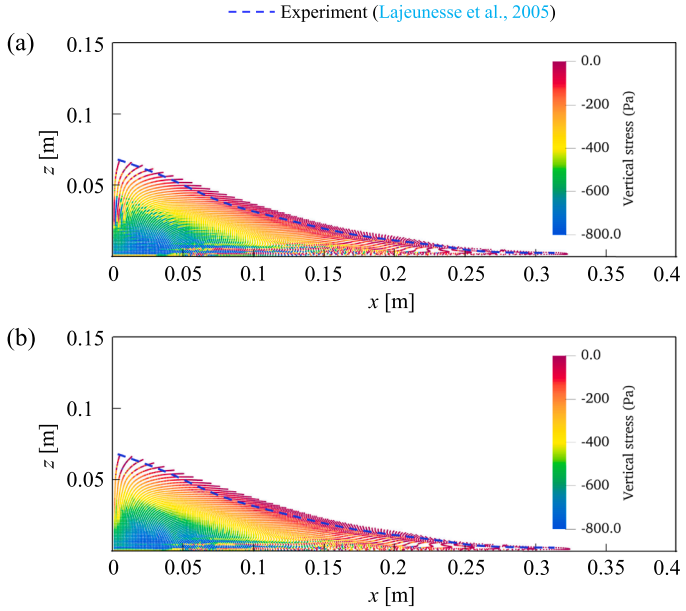

Fig. 12. Column collapse: comparison of vertical stress at a stable state (a) without and (b) with hybrid strain smoothing.

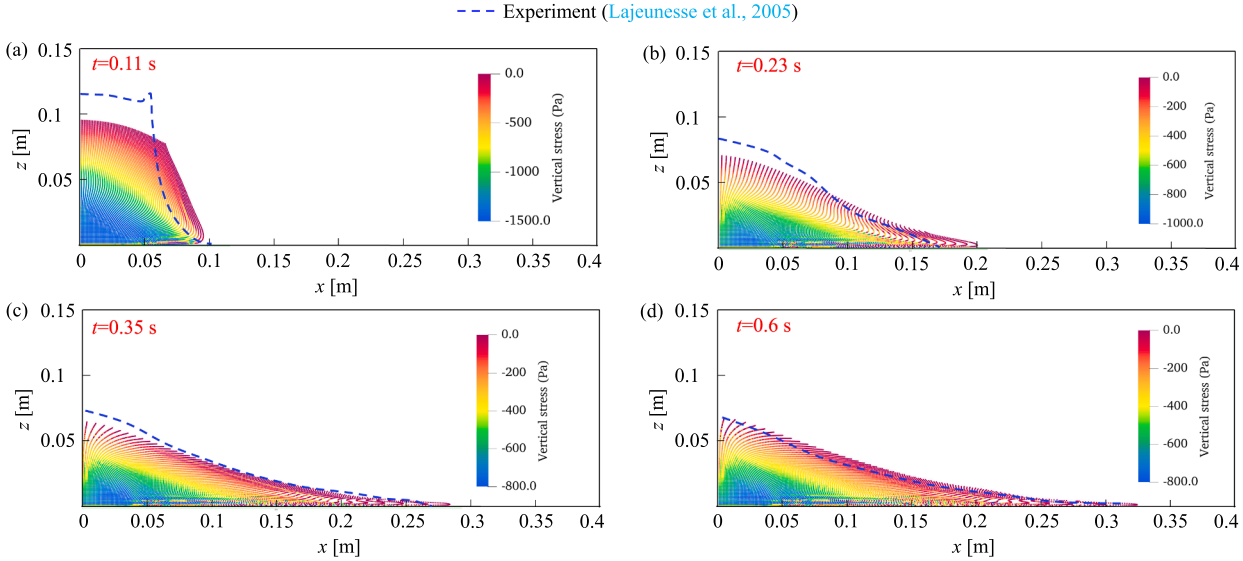

Fig. 13. Comparison of configuration evolution with experimental results: (a) $t = 0.11$ s; (b) $t = 0.23$ s; (c) $t = 0.35$ s; (d) $t = 0.6$ s.

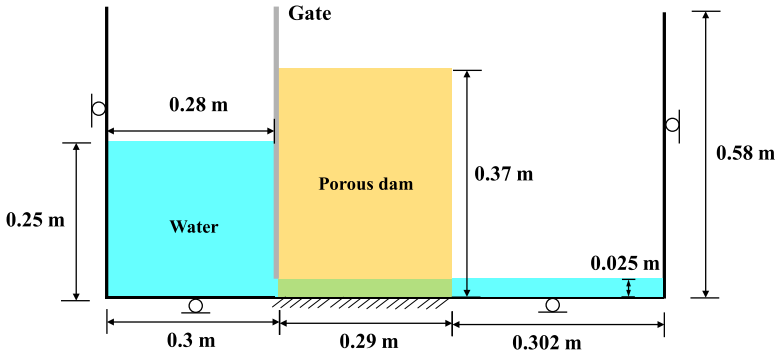

Fig. 14. Flow passing through a porous dam: initial configuration and boundary conditions.

in the simulation versus the finite removal time in physical experiments. Nevertheless, frictional effects at the base gradually diminish this discrepancy, ultimately leading to convergent final states. The overall agreement between numerical and experimental results confirms the accuracy and robustness of the implemented hybrid strain smoothing approach for solid phase modeling.

5. Numerical examples

5.1. Flow passing through a porous dam

This study utilizes benchmark experimental data from Liu et al. [114], employing simplified configurations with comprehensive measurements that have become a standard reference for validating porous media flow models. The research specifically examines the spatiotemporal evolution of the free water surface across the porous medium interface. The experimental apparatus (see Fig. 14) comprises a glass tank measuring 0.892 m in length $\times$ 0.58 m in height, centrally positioned with a porous dam of 0.29 m width and 0.37 cm thickness. Water flow is initiated by rapid removal of a left-side gate mechanism, with continuous monitoring of free surface elevation dynamics throughout the experiment.

The porous dam is characterized as an isotropic linear elastic material with the following phase-specific properties: solid grain density $\rho_s = 2500\,\mathrm{kg/m^3}$, Young's modulus $E_s = 5\,\mathrm{MPa}$, Poisson's ratio $\nu = 0.3$. The initial porosity n_0 is 0.49, and particle diameter 0.0159 m yields an initial permeability $k_0 = 7.5$ m/s, calculated using the Kozeny-Carman equation. The water phase is characterized by density $\rho_w = 1000\,\mathrm{kg/m^3}$, bulk modulus $K_w = 10\,\mathrm{MPa}$, and dynamic viscosity $\mu_w = 0.001\,\mathrm{Pa{\cdot}s}$. Numerical discretization employs a uniform square grid $h = 0.005$ m with 2×2 particle initialization per element, generating 17,168 material points for the solid domain and 13,640 for the water domain. The simulation has a total duration of 2.0 s and the time step is set to $\Delta t = 1 \times 10^{-5}$ s. The blending coefficient is set to $\beta = 0.05$.

Fig. 15 presents a comparative analysis between numerical predictions and experimental measurements, denoted by black hollow circles at sequential time intervals. The simulation captures key physical phenomena including initial water infiltration into the dam, flow retardation due to porous medium resistance evidenced by elevated front water levels at $t = 0.4$ s, and subsequent surface stabilization. Numerical results show good agreement with experimental data and exhibit smooth pressure field, while with some discrepancies in the liquid surface elevation inside the dam during the first three snapshots. The observed discrepancies primarily originate from differing gate removal mechanisms [114]. While the simulation assumes instantaneous gate removal with uniform fluid release, the physical experiment involves manual operation that preferentially accelerates bottom-water flow [115]. Notably, predictive accuracy enhances progressively with time, achieving high-fidelity reproduction of later-stage flow patterns. This systematic validation confirms the proposed stabilized two-point, two-phase formulation's capability to accurately resolve dynamic hydro-mechanical coupling.

We also compare the pressure results obtained using the explicit standard MPM with various basis functions. As illustrated in Fig. 16(a), significant pressure oscillations are observed when GIMP basis functions are employed. In contrast, the use of cubic B-spline basis functions, depicted in Fig. 16(b), notably reduces these oscillations. With the stabilization techniques proposed in this study, a much smoother pressure field is achieved, as shown in Fig. 16(c), compared to the results from the standard MPM. To evaluate pressure oscillations within the pressure field, the Laplacian of pressure, $\nabla^2 p$, is computed at the positions of the material points in Fig. 16. Additionally, the standard deviation of the $\nabla^2 p$ field is calculated to provide a quantitative assessment of pressure oscillations. In comparison, the $\nabla^2 p$ values in this study exhibit a smaller standard deviation, demonstrating the effectiveness of the proposed stabilized two-point, two-phase formulation in mitigating pressure oscillations within the explicit MPM framework.

5.2. Submerged landslide

This study utilizes the benchmark submarine landslide experiment conducted by Rzadkiewicz et al. [116] to validate the hydro-mechanical coupling performance of the proposed stabilized two-point two-phase MPM formulation, with particular focus on its ability to capture water wave generation induced by subaqueous slope failures. The selected experimental configuration has been

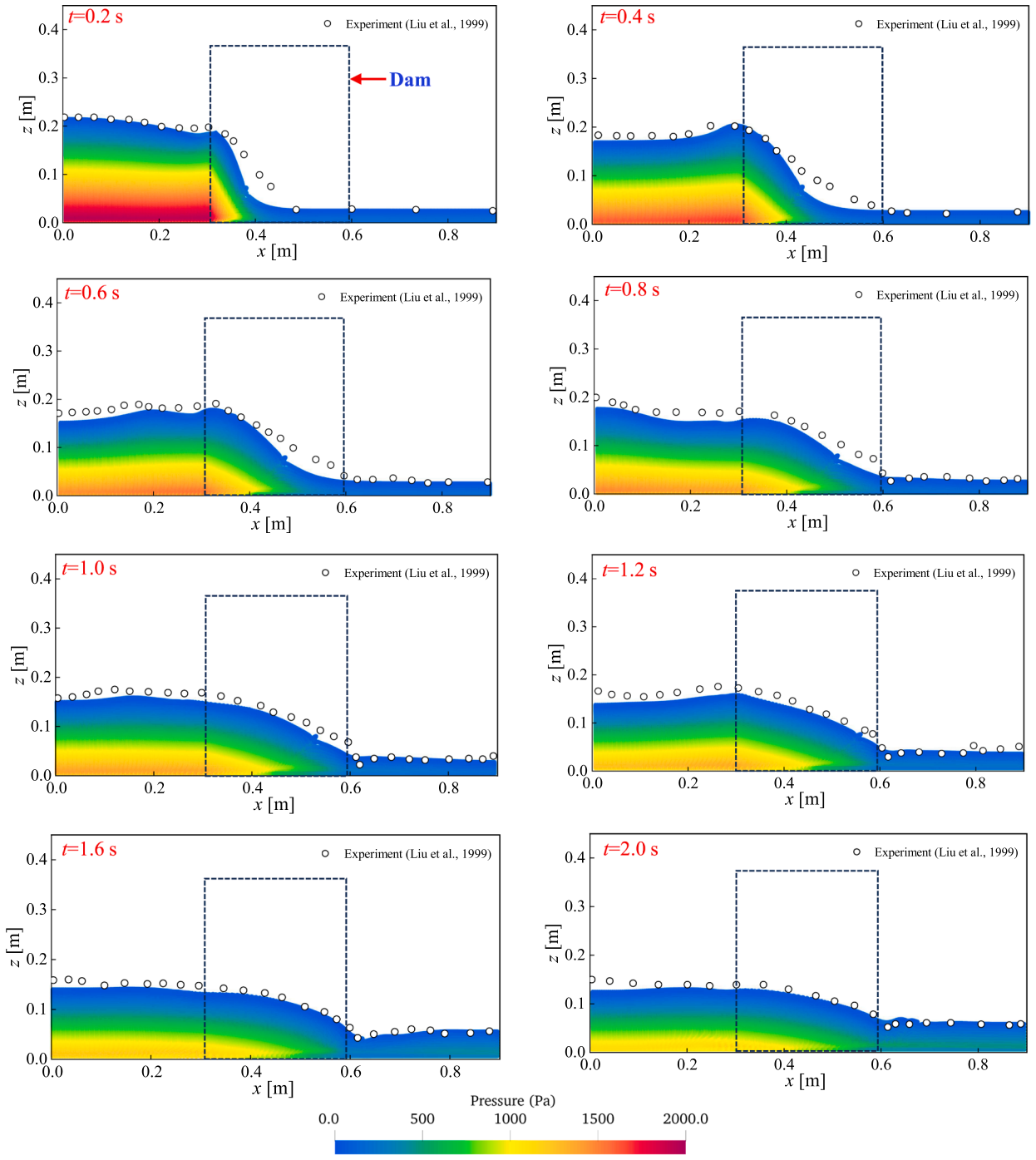

Fig. 15. Flow passing through a porous dam: comparison of configuration evolution with experimental results at different time instants. The dam is simply displayed as a dashed rectangle due to its negligibly small deformation throughout the process.

rigorously validated through various numerical approaches, including SPH [117], PFEM [115], semi-implicit MPM [45], and coupled CFD-MPM [46].

The experimental setup (see Fig. 17) consists of a 4 m long flume containing water to a depth of 1.6 m. A triangular sand mass is placed on a 45° inclined plane at the right end of the tank, initially submerged 0.1 m below the water surface and held in place by a vertical gate. All boundaries, including the slope interface, are treated as frictionless. The system first reaches hydrostatic equilibrium

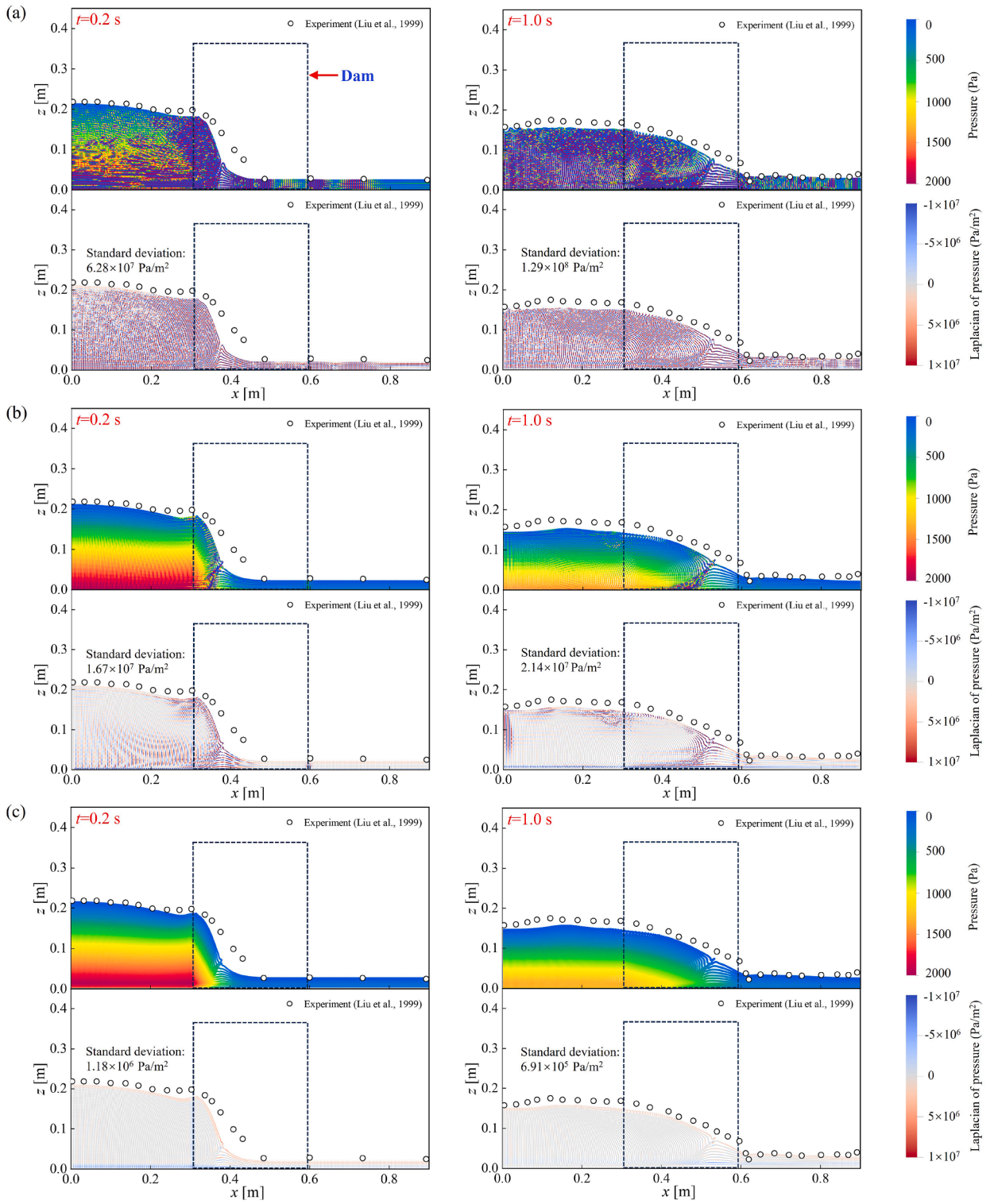

Fig. 16. Flow passing through a porous dam: comparison of pressure contours and the Laplacian of pressure $\nabla^2 p$ fields using explicit standard MPM with (a) GIMP basis functions, (b) cubic B-spline basis functions, and (c) the proposed method.

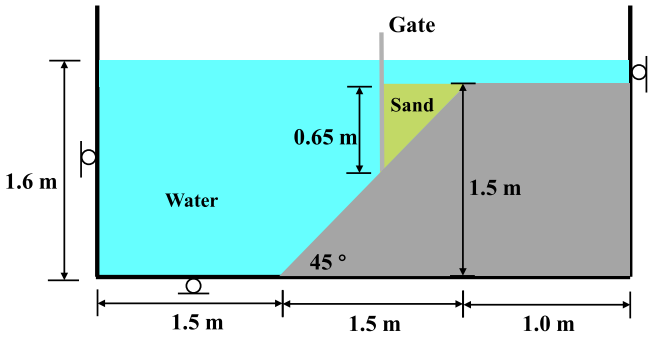

Fig. 17. Submerged landslide: initial configuration and boundary conditions.

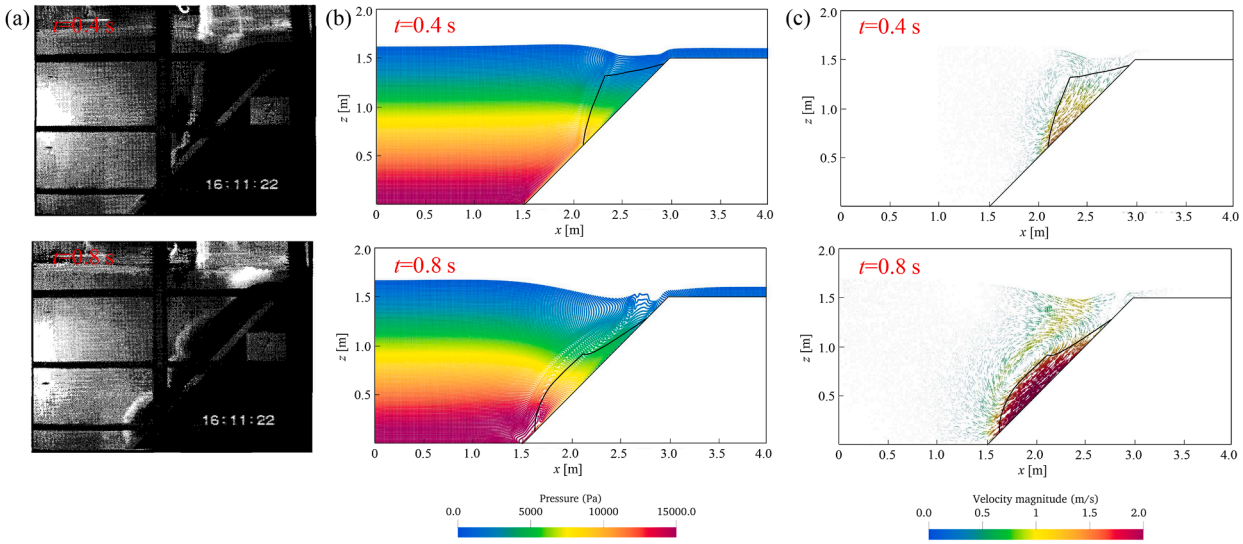

Fig. 18. Submerged landslide: (a) experimental results [116]; (b) numerical pressure contours; (c) numerical velocity field.

under gravity before the gate is rapidly removed, triggering sand mass motion and consequent water surface disturbances. Numerical discretization employs a uniform square grid with element size $h = 0.025$ m, using a 2×2 particle configuration for both phases. This results in 1378 solid material points and 24,220 water material points. The simulation parameters include a time step $\Delta t = 1 \times 10^{-5}$ s and blending coefficient $\beta = 0.01$.

Consistent with previous work [45], the granular material is modeled as a Mohr-Coulomb continuum with the following properties: solid grain density $\rho_s = 2650\,\mathrm{kg/m^3}$, Young's modulus $E_s = 5$ MPa, Poisson's ratio $\nu = 0.3$, friction angle $\phi = 10°$, zero dilation angle ($\psi = 0$), and zero cohesion $c = 0$. The water phase is characterized by density $\rho_w = 1000\,\mathrm{kg/m^3}$, bulk modulus $K_w = 20$ MPa, and dynamic viscosity $\mu_w = 0.001$ Pa·s. Initial conditions include porosity $n_0 = 0.4$ and mean particle diameter $d_{50} = 0.006$ m, yielding a Darcy's permeability $k_0 = 0.43$ m/s through the Kozeny-Carman relation.

Fig. 18 presents comparative snapshots of the submerged landslide at $t = 0.4$ s and $t = 0.8$ s, showing both experimental observations and numerical simulations of water pressure and flow velocity fields around the sand mass, denoted by black contours. Initial sand movement at $t = 0.4$ s exhibits minimal displacement following gate removal, while substantial deformation becomes evident by $t = 0.8$ s. The stabilized two-point two-phase MPM accurately reproduces both the evolving sand configuration and the developing water vortices, as shown in Fig. 18(c). The pressure field in Fig. 18(b) demonstrates the method's effectiveness in preventing volumetric locking, maintaining smooth pressure distributions during initial stages. However, the progressive movement of sand induces localized pressure oscillations, as shown in Fig. 19(a). By employing the δ-correction, the standard deviation of $\nabla^2 p$ is reduced by nearly 45%, which means these oscillations can be further mitigated, resulting in improved stability of the pressure field, as depicted in Fig. 19(b).

The stress field evolution is shown in Fig. 20, comparing experimental soil profiles with various numerical approaches. While previous simulations [46,115] display stress oscillations, our hybrid strain smoothing technique produces smoother stress distributions in Fig. 20(a), demonstrating enhanced capability in addressing dynamic locking. Comparative sand profiles in Fig. 20(b) reveal excellent agreement at $t = 0.4$ s across other methods [45,46,115–117], though these numerical approaches under-predict displacement at $t = 0.8$ s, likely due to unmodeled liquefaction effects in the constitutive formulation [115]. Free surface evolution is quantitatively

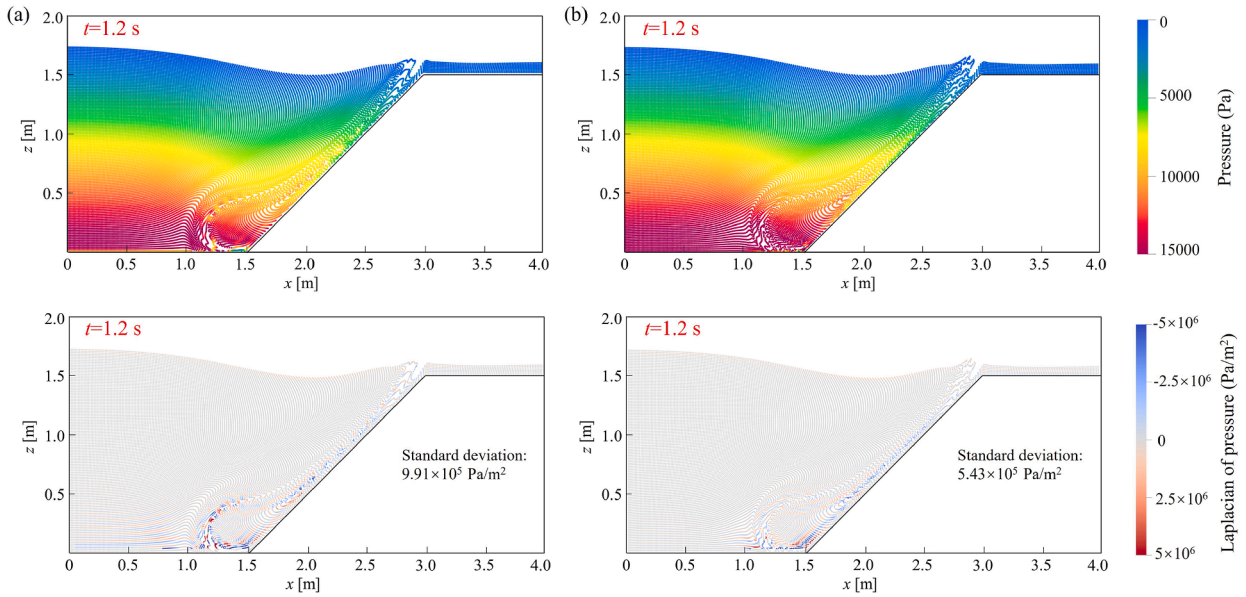

Fig. 19. Submerged landslide: pressure contours and $\nabla^2 p$ fields at $t = 1.2$ s performed (a) without and (b) with δ-correction.

validated in Fig. 21, showing strong correspondence between our predictions, experimental measurements, and reference numerical solutions at both $t = 0.4$ s and $t = 0.8$ s. This comprehensive agreement confirms the reliability of the proposed coupled framework in capturing essential submarine landslide dynamics.

5.3. Subaerial granular collapse

In this subsection, we employ the proposed stabilized MPM to investigate water wave generation induced by granular column collapse. Our simulation results are systematically compared with experimental data from Zhao et al. [118]. The numerical study replicates a laboratory experiment where water waves are generated through the collapse of a dry granular column into water, as illustrated in Fig. 22.

The experimental configuration comprises a glass tank with dimensions 2 m in length × 0.5 m in height × 0.15 m in width. The granular column spans the tank's width, ensuring that both the resulting impulse wave and granular motion conform to a 2D plane strain condition. Initially, the granular column is positioned at the base and restrained by a left-side gate. The column has an initial height $H_{s0} = 0.145$ m and width $L_{s0} = 0.08$ m, while the water depth is maintained at $h_{w0} = 0.055$ m, aligning the column's base with the water surface. Upon gate release, the column collapses into the water, generating waves.

For numerical simulation, the computational domain is discretized using a square grid with element size $h = 0.00125$ m. A 2×2 particle configuration is applied to both solid and water phases, yielding 29,696 material points for the solid phase and 129,184 for the water phase. The time step is set to $\Delta t = 1 \times 10^{-5}$ s. Gravitational acceleration ($g = 9.81$ m/s^2) acts on both phases, and a temporary gate facilitates granular column consolidation. Slip-wall conditions are imposed at the left and right boundaries, while the bottom surface is treated as rough with a friction coefficient $\mu = 0.36$ (derived from $\tan\phi$). After the granular column stabilizes under gravity, the gate is removed to initiate collapse.

The granular material is modeled as a Mohr-Coulomb continuum, adopting material parameters from Zhao et al. [118], with the following material properties: solid grain density $\rho_s = 2500$ kg/m^3, Young's modulus $E_s = 10$ MPa, Poisson's ratio $\nu = 0.3$, and a friction angle $\phi = 20°$. Both the dilation angle ψ and cohesion c are set to 0. The initial porosity is $n_0 = 0.43$, and the mean particle diameter is $d_{50} = 0.005$ m, resulting in an intrinsic permeability of $k_0 = 0.4$ m/s, as calculated using the Kozeny-Carman relation. The water phase is characterized by density $\rho_w = 1000$ kg/m^3, bulk modulus $K_w = 2$ MPa, and dynamic viscosity $\mu_w = 0.001$ Pa·s.

Fig. 23 compares numerical and experimental results, with the black line delineating the granular material configuration. The collapsing granular column generates multiple waves that propagate forward, consistent with experimental observations in Fig. 23. Concurrently, water infiltrates the initially dry granular region, progressively saturating the solid particles. The pressure field remains smooth and stable throughout, demonstrating the robustness of the stabilized MPM in handling large deformations and complex solid-fluid interactions.

Fig. 24 illustrates the evolution of the solid phase configuration and stress field. At $t = 0.1$ s, the stress distribution is smooth, though interactions with the rough base induce minor oscillations, as shown in Fig. 24(c) and (d). These oscillations arise from granular-bottom friction and water infiltration, introducing additional complexity to stress stabilization.

Fig. 25 depicts the granular front length along the bottom and the wave amplitude relative to the initial water height. The granular front elongation rate decelerates over time, while the wave amplitude stabilizes. A slight underestimation of the granular front length

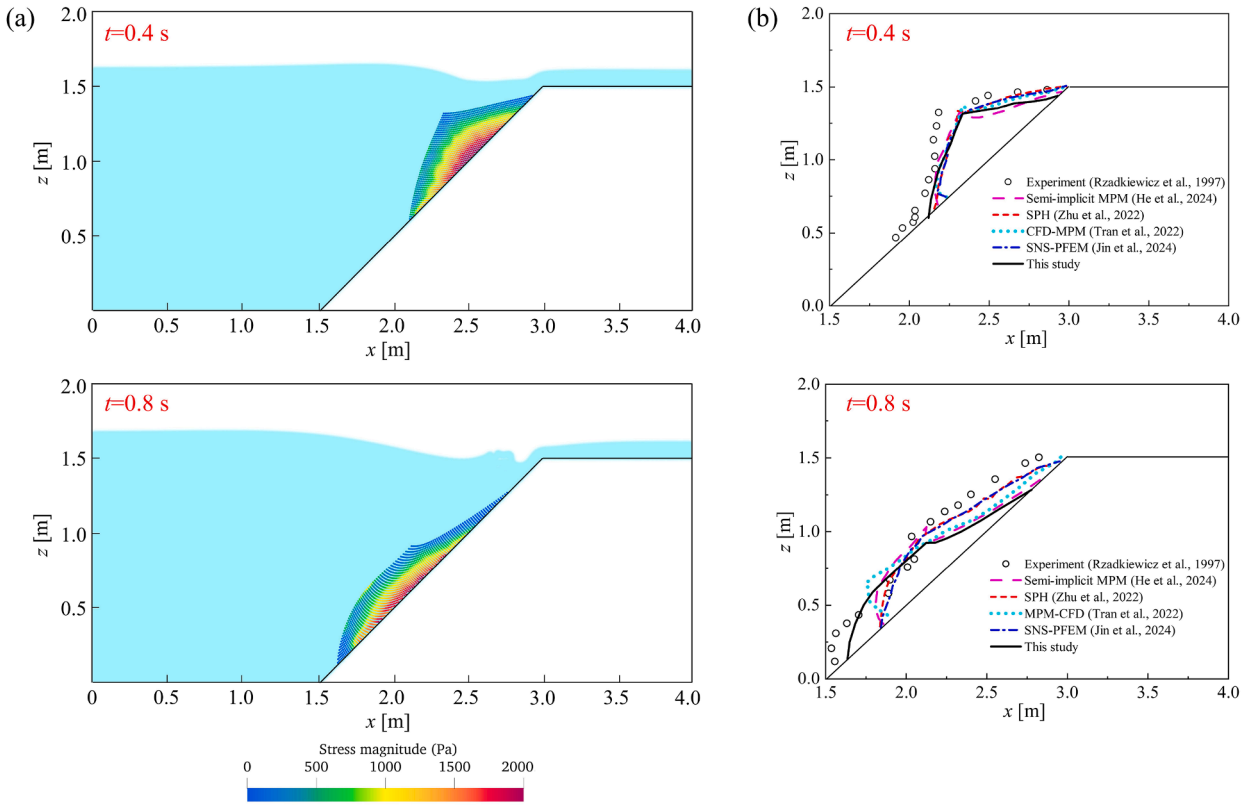

Fig. 20. Submerged landslide: (a) solid stress; (b) granular configuration.

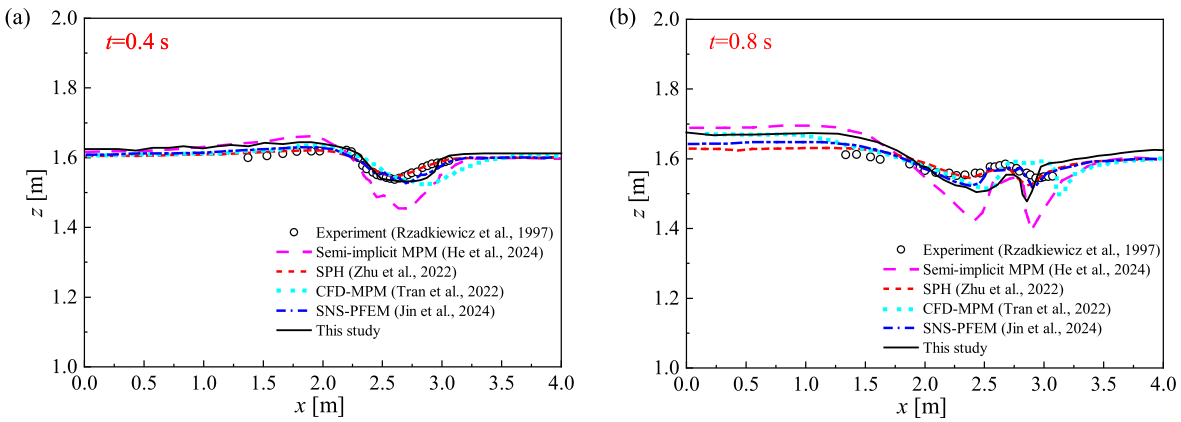

Fig. 21. Submerged landslide: experimental and simulated results of the free fluid surface profile from different methods at (a) $t = 0.4$ s and (b) $t = 0.8$ s.

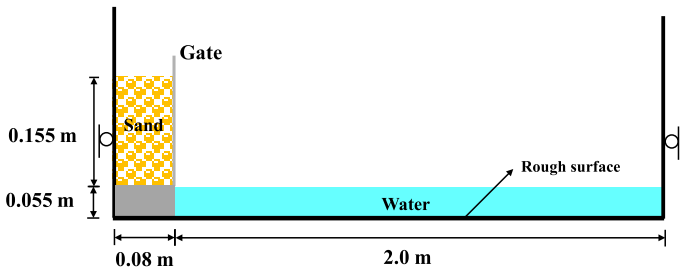

Fig. 22. Subaerial granular collapse: initial configuration and boundary conditions.

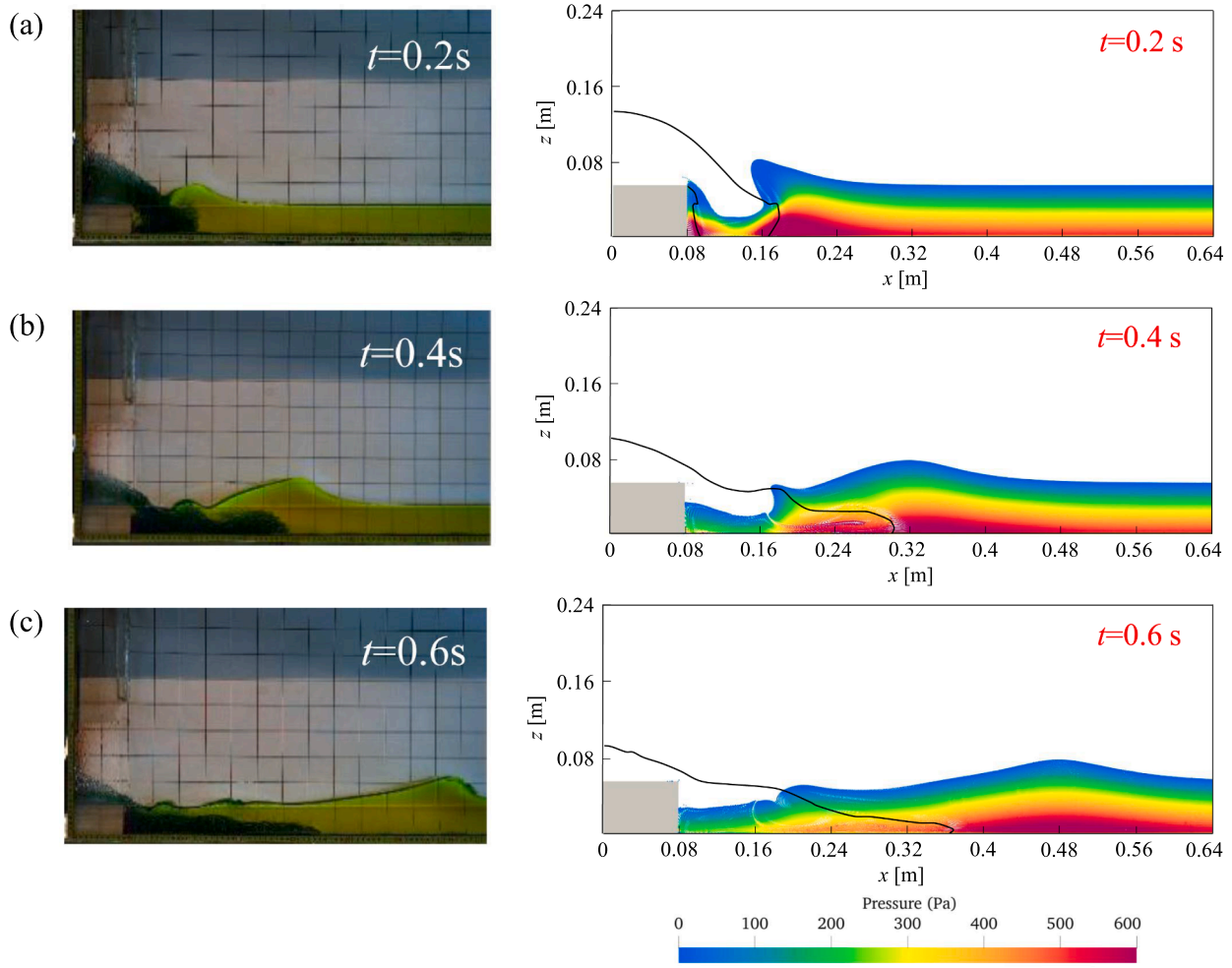

Fig. 23. Subaerial granular collapse: (a) experimental results; (b) numerical pressure contours.

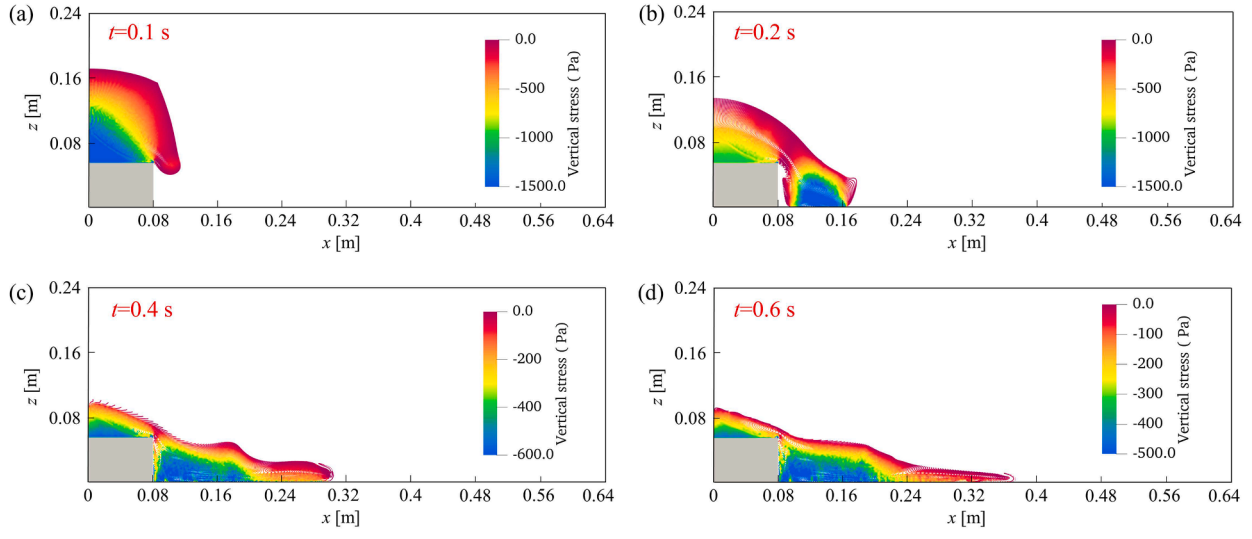

Fig. 24. Subaerial granular collapse:(a) $t = 0.1$ s; (b) $t = 0.2$ s; (c) $t = 0.4$ s; (d) $t = 0.6$ s.

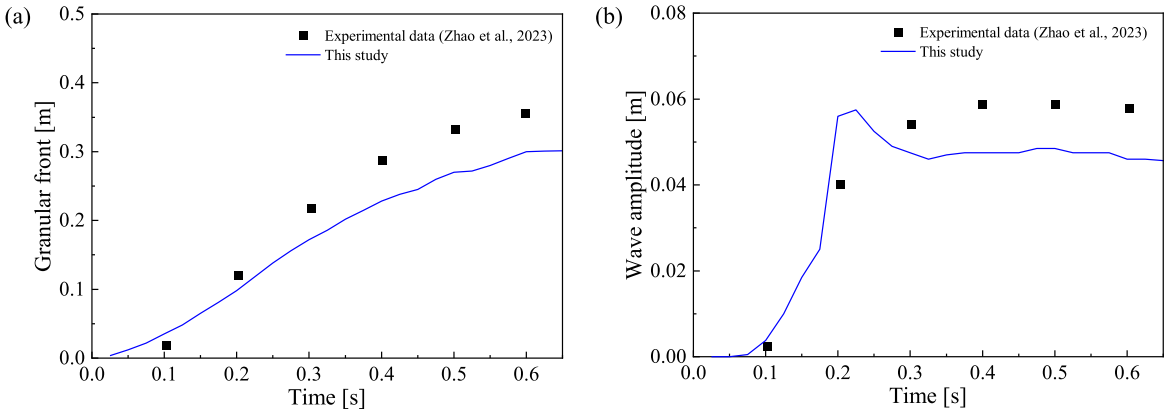

Fig. 25. Subaerial granular collapse: comparison of (a) granular front length and (b) wave amplitude with experimental results.

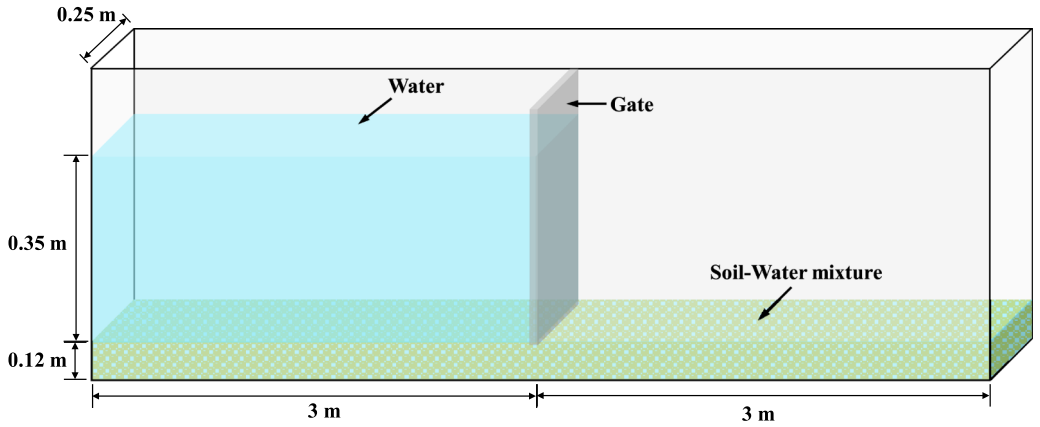

Fig. 26. Intense bedload by dam-break: problem geometry.

in simulations may stem from the constitutive model's omission of liquefaction-induced strength reduction. Notably, Fig. 25(b) reveals a transient peak in wave amplitude, likely attributable to energy dissipation during water infiltration. As infiltration diminishes and wave propagation continues, the amplitude stabilizes.

5.4. Intense bedload by dam-break

Finally, we evaluate the performance of the proposed approach on 3D large-deformation problems by simulating a laboratory dam-break experiment [119]. The experimental geometry is illustrated in Fig. 26. The setup consists of a rectangular flume measuring 6.0 m in length and 0.25 m in width. The soil bed comprises cohesionless cylindrical PVC grains saturated with water. Initially, a gate positioned at the mid-section of the tank retains a water reservoir with a depth of 0.35 m. Upon reaching equilibrium, the gate is instantaneously removed, allowing the water to flow over the granular bed.

For the numerical simulation, a square grid with an element size of $h = 0.03$ m is used to discretize the computational domain. Both the solid and water phases are represented by a $2 \times 2 \times 2$ particle configuration, resulting in 51,200 material points for the solid phase and 124,800 for the water phase. The time step is set to $\Delta t = 1 \times 10^{-5}$ s. Gravitational acceleration ($g = 9.81\,\mathrm{m/s^2}$) is applied to both phases, and a temporary gate is used to facilitate initial consolidation. The base boundary of the bed is fully fixed, while the side boundaries are supported by rollers. Once the system reaches a steady state under gravity, the gate is removed to initiate the dam-break process.

The soil is modeled using the Mohr-Coulomb constitutive model using material parameters based on the experimental setup in Spinewine and Capart [119]. The soil material properties are as follows: grain density $\rho_s = 1580\,\mathrm{kg/m^3}$, Young's modulus $E_s = 10$ MPa, Poisson's ratio $\nu = 0.3$, , and friction angle $\phi = 38°$. Both the dilation angle ψ and cohesion c are set to zero. The initial porosity is

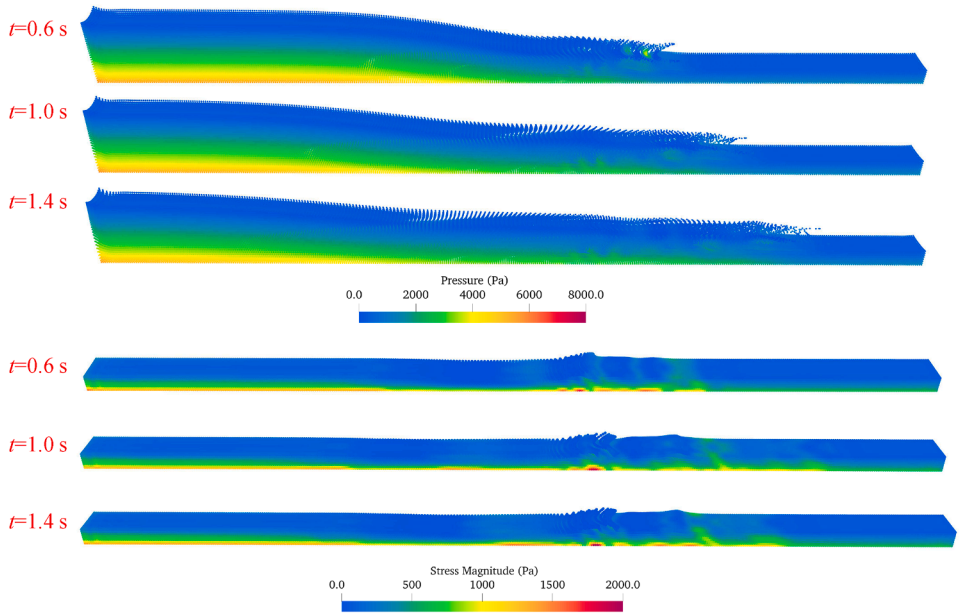

Fig. 27. Intense bedload by dam-break: evolution of water pressure and soil stress at different times.

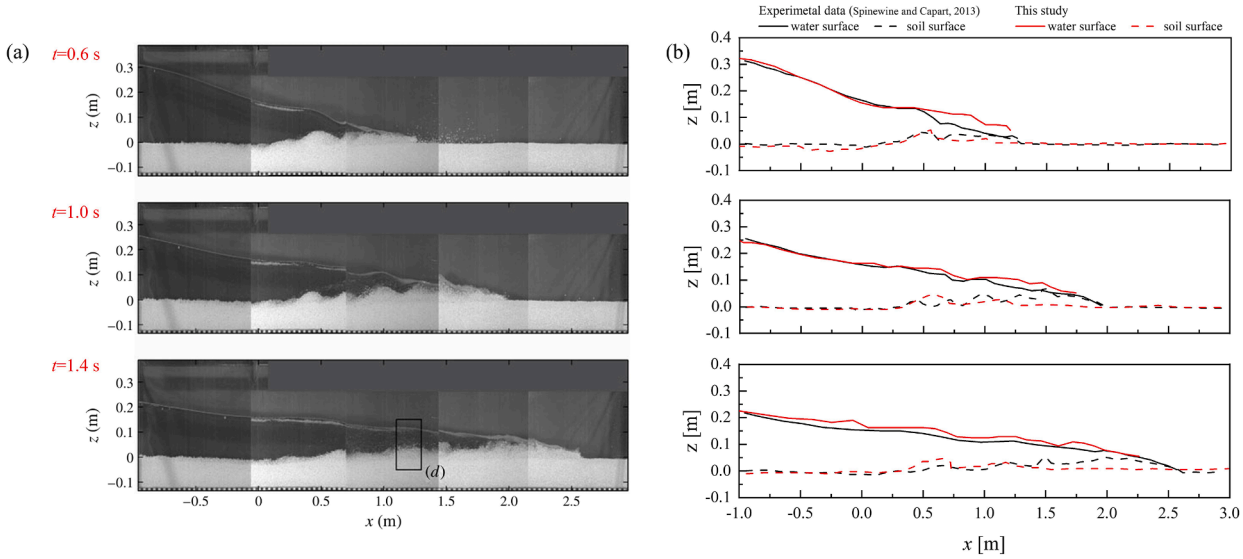

Fig. 28. Intense bedload by dam-break: comparison of water and soil surface profiles between (a) experimental data and (b) this study.

$n_0 = 0.42$, and the mean particle diameter is $d_s = 0.0039$ m. The water phase is characterized by density $\rho_w = 1000\,\mathrm{kg/m^3}$, bulk modulus $K_w = 10$ MPa, and dynamic viscosity $\mu_w = 0.001$ Pa·s.

Fig. 27 presents the simulation snapshots of the intense sediment transport process. The free-surface water flows over the bed, driving the movement of solid particles. As time progresses, the water front propagates further, inducing large deformations in the soil bed. Throughout the process, the water pressure field exhibits a smooth distribution along the bed. For the solid phase, the stress field is generally smooth. However, local oscillations occur near the water flow front. These oscillations arise from violent scouring interactions between the soil and water, which introduce additional complexity to stress stabilization.

To further validate the accuracy of our method, Fig. 28 compares the water and soil surface profiles obtained from experiments and numerical simulations. The results demonstrate good agreement for both phases, although some discrepancies are observed near

the water front. Notably, in the experiments, soil liquefaction was observed, while is not accounted for in the present model. This omission likely contributes to the discrepancies with the experimental results.

6. Conclusions

This study presents a stabilized explicit two-point two-phase MPM framework for simulating solid-fluid coupling problems in porous media. Volumetric locking in the fluid phase is effectively mitigated through dual volume averaging applied to both deformation gradients and pressure, which utilizes cubic B-spline basis functions for particle-grid mapping. Additionally, a hybrid strain smoothing technique is introduced for the solid phase to reduce stress oscillations by implementing cell-based and node-based smoothing for deviatoric and volumetric strain, respectively. To counteract accuracy loss at low grid resolutions associated with the APIC mapping scheme, the AFLIP strategy is introduced. Furthermore, to minimize quadrature errors caused by particle clustering, the δ-correction method is applied to the fluid phase, enhancing the stability of the numerical solution.

A series of benchmark tests, including 1D and 2D consolidation problems, single-phase dynamic problems, flow passing through a porous dam, submerged granular landslides, subaerial granular collapses, and 3D intense bedload by dam-break are conducted to verify and validate the proposed framework. The results show good agreement with experimental data and numerical results from other studies. Notably, the proposed stabilized explicit MPM scheme maintains numerical stability and effectively smooths stress, even in challenging dynamic scenarios. This approach offers a promising avenue for large-deformation simulations involving solid-fluid coupling.

Computational efficiency is a key challenge when extending the proposed method to 3D problems. Although this study utilizes OpenMP for parallel computing to enhance computational efficiency, future work will explore GPU computing [70,120] for 3D simulations. Additonally, the underprediction of this framework for the granular-fluid flows involving undrained loading indicates the necessity of advanced constitutive models for capturing transient pore-pressure feedback and liquefaction, which will be a future direction. Futhermore, further research will aim to incorporate multi-physical fields, such as temperature, into the proposed MPM framework to enhance the model's comprehensiveness.

CRediT authorship contribution statement

Zhang Cheng: Writing – original draft, Visualization, Validation, Software, Methodology; **Shiwei Zhao:** Writing – review & editing, Supervision, Funding acquisition; **Hao Chen:** Writing – review & editing; **Jidong Zhao:** Writing – review & editing, Supervision, Funding acquisition.

Data availability

The simulation scripts will be made available upon request.

Data availability

No data was used for the research described in the article.

Declaration of competing interest

The authors declare that they have no known competing financial interests or personal relationships that could have appeared to influence the work reported in this paper.

Acknowledgments

This work was financially supported by the National Natural Science Foundation of China (Project No. 52439001), the Research Grants Council of Hong Kong (GRF Projects No. 16214525, No. 16206322 and No. 16211221, CRF Project No. C7085-24G, and TRS Project No. T22-606/23-R and No. T22-607/24N), and the State Key Laboratory of Climate Resilience for Coastal Cities (SKLCRCC) (via Project ITC-SKLCRCC26EG01). Any opinions, findings, conclusions or recommendations expressed in this material are those of the authors and do not necessarily reflect the views of the funding agencies.

Appendix A.

The hybrid strain smoothing technique reduces stress oscillations and enhances numerical stability, but it may also introduce numerical dissipation. To assess the impact of potential dissipation on numerical accuracy, we further compare the stress results from the 2D Cryer's problem. As shown in Fig. A.1, the radial stress results obtained with and without hybrid smoothing are in excellent agreement. In the hybrid smoothing scheme, a double mapping is employed to smooth the volumetric strain for stabilized pressure computation, while the deviatoric strain is replaced with its cell-centered counterpart. This differentiated treatment of volumetric and deviatoric strain helps mitigate dissipation while preserving numerical accuracy.

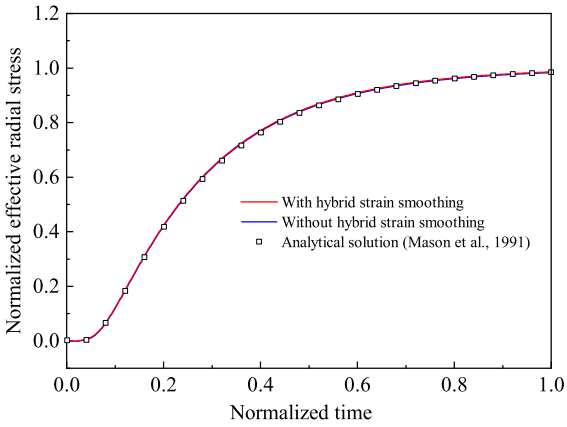

Fig. A.1. 2D Cryer's problem: comparison of radial stress at the center with $\nu = 0.3$.

Appendix B.

To validate the conservation of fluid volume, we compare the water depth at $t = 4$ s, when the flow has reached a nearly steady state. As shown in Fig. A.2, the water depth simulated using the proposed stabilized MPM is close to that obtained without dual volume averaging. This indicates that the introduction of the dual volume averaging method does not lead to significant volume loss. The analytical final water depth, computed from the initial volume and porosity following [117], is represented by the red dashed line in Fig. A.2. The numerical water depth shows good agreement with the analytical solution, demonstrating satisfactory volume conservation throughout the entire simulation.

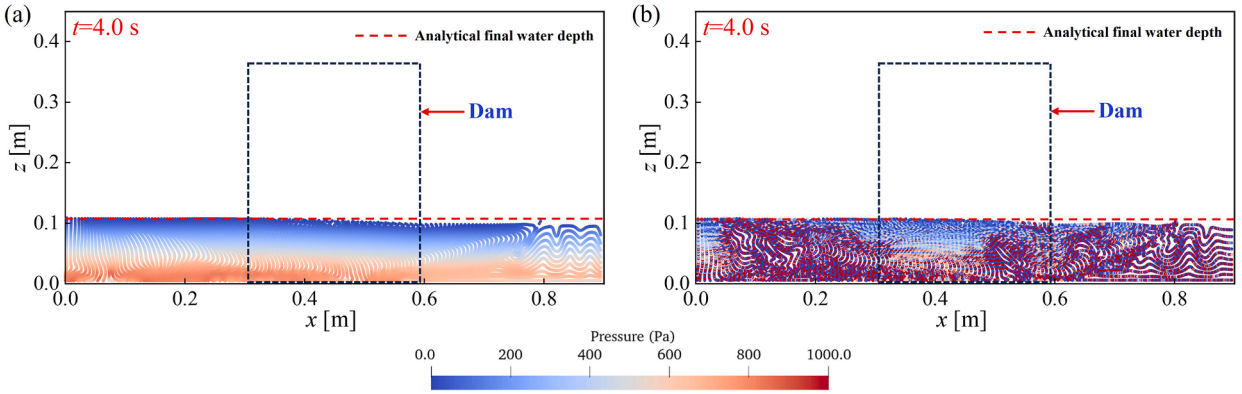

Fig. A.2. Flow passing through a porous dam: comparison of water depth at $t = 4$ s using explicit MPM (a) with and (b) without dual volume averaging.

Appendix C.

Following the δ-correction operation proposed by Baumgarten et al. [59], particle positions are artificially adjusted to improve spatial distribution while maintaining material and state properties unchanged. However, retaining previous-time-step state variables (e.g., velocity $\boldsymbol{v}_{fp}$, stress $\boldsymbol{\sigma}_{fp}$, porosity n, volume V_{fp}) for relocated particles may violate the continuity of physical fields. To address this issue, we implement a modified δ-correction scheme that interpolates physical variables ϕ_{fp} for relocated particles using nodal values ϕ_i as follows:

$$\phi_{fp}^{k+1} = \sum_i w_i(\boldsymbol{x}'_{fp})\phi_i^{k+1} \tag{C.1}$$

As shown in Fig. A.3, the pressure contours and particle distribution obtained using the modified δ-correction technique at $t = 1.2$ s are similar to previous results for the submerged landslide. This indicates that the choice not to update the state variables of the shifted material points does not significantly affect numerical stability and particle distribution.

Fig. A.4 further presents the energy evolution of the fluid phase. Both the δ-correction and modified δ-correction techniques show good agreement in kinetic and potential energy evolution, which corresponds to the observations in Fig. A.3. The error introduced by

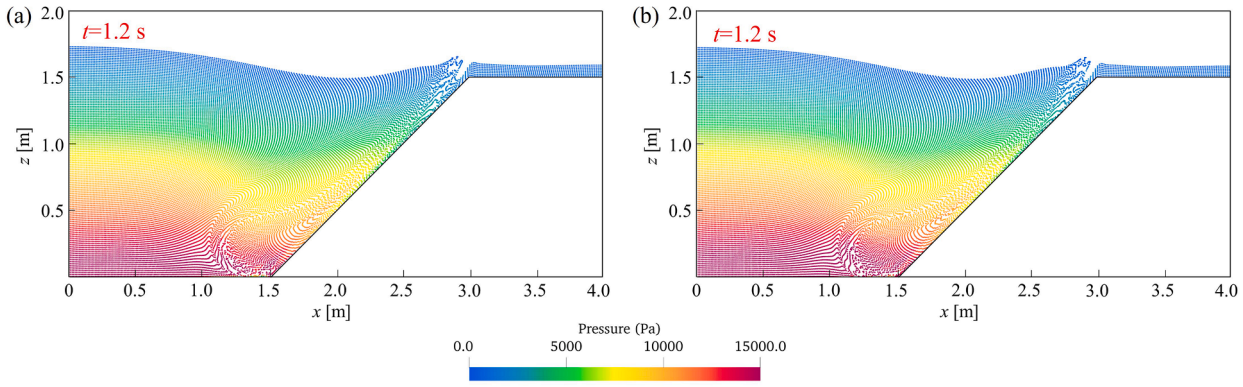

Fig. A.3. Submerged landslide: pressure contours at t = 1.2 s performed (a) with δ-correction and (b) modified δ-correction.

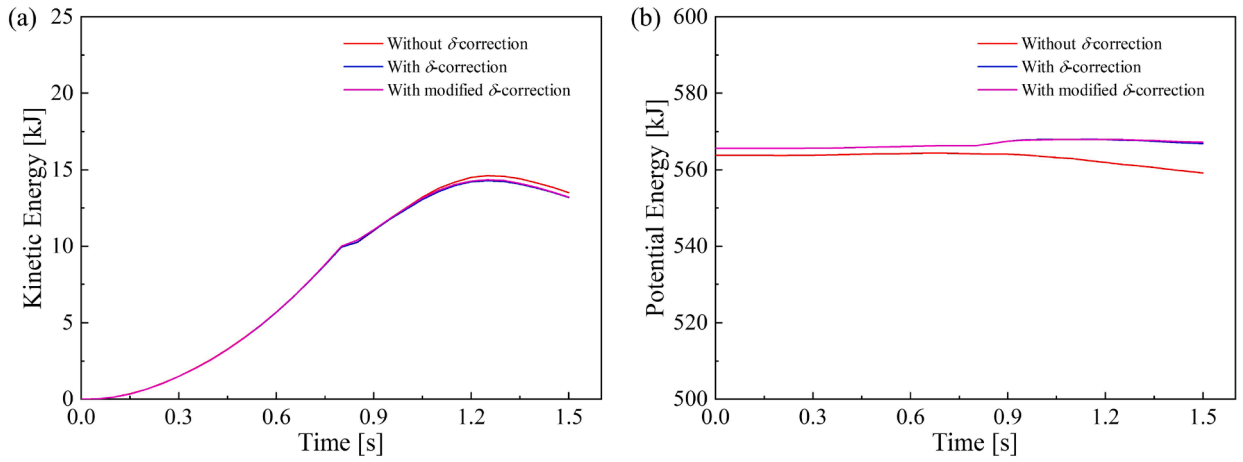

Fig. A.4. Submerged landslide: comparison of (a) kinetic energy and (b) gravitational potential energy of the fluid phase with and without the δ-correction technique.

not updating the state variables is proportional to the step length [59]. In the present case, the time step is 10^{-5} s, and the maximum shifting distance for fluid material points in each step is smaller than 0.1 times the element size. Thus, the discrepancy between the δ-correction and modified δ-correction is small. On the other hand, the use of δ-correction leads to some kinetic energy dissipation, with a maximum dissipation of approximately 2.4% as shown in Fig. A.4(a). Due to particle shifting, clumped material points separate, resulting in an increase in gravitational potential energy, as seen in Fig. A.4(b), with a maximum increase of about 1.4%. Therefore, while δ-correction slightly affects energy transfer, its benefits in improving particle distribution and numerical stability make it an acceptable approach.

References

[1] L. Chen, Y. Duan, M. Liu, C. Zhao, Slip flow of coal water slurries in pipelines, Fuel 89 (5) (2010) 1119–1126.
[2] M. Pailha, O. Pouliquen, A two-phase flow description of the initiation of underwater granular avalanches, J. Fluid Mech. 633 (2009) 115–135.
[3] J. Fang, L. Wang, Y. Hong, J. Zhao, Influence of solid-fluid interaction on impact dynamics against rigid barrier: CFD-dem modelling, Géotechnique 72 (5) (2022) 391–406.
[4] Y. Kong, M. Guan, Hydro-mechanical simulations aid demand-oriented design of slit dams for controlling debris flows, debris avalanches and rock avalanches, Eng. Geol. 326 (2023) 107314.
[5] K. Soga, E. Alonso, A. Yerro, K. Kumar, S. Bandara, Trends in large-deformation analysis of landslide mass movements with particular emphasis on the material point method, Géotechnique 66 (3) (2016) 248–273.
[6] K.-L. Zhao, L.-C. Qiu, Y. Liu, Two-layer two-phase material point method simulation of granular landslides and generated tsunami waves, Phys. Fluids 34 (12) (2022) 123312.
[7] C. Harbitz, S. Glimsdal, F.L. vholt, V. Kveldsvik, G. Pedersen, A. Jensen, Rockslide tsunamis in complex fjords: from an unstable rock slope at åkerneset to tsunami risk in western norway, Coastal Eng. 88 (2014) 101–122.
[8] H. Yang, Z. Guo, Y. Li, H. Wang, Y. Dou, Experimental study on microbubble drag reduction on soil-steel interface, Appl. Ocean Res. 116 (2021) 102891.
[9] Y. Li, Z. Guo, L. Wang, Y. Zhu, S. Rui, Field implementation to resist coastal erosion of sandy slope by eco-friendly methods, Coastal Eng. 189 (2024) 104489.
[10] R. Feng, G. Fourtakas, B.D. Rogers, D. Lombardi, Modelling internal erosion using 2D smoothed particle hydrodynamics (SPH), J. Hydrol. 639 (2024) 131558.
[11] S. Mei, M. Peng, H. Chen, Y. Li, Evaluation of drainage conditions during uplift using a new dimensionless velocity, Ocean Eng. 351 (2026) 124376.
[12] P.A. Cundall, O.D. Strack, A discrete numerical model for granular assemblies, geotechnique 29 (1) (1979) 47–65.
[13] S. Zhao, Z. Lai, J. Zhao, Leveraging ray tracing cores for particle-based simulations on gpus, Int. J. Numer. Methods Eng. 124 (3) (2023) 696–713.

[14] Z. Yang, Z. Guo, H. Liu, J. Zhang, W. Xu, Y. Li, Early strength at hour level and influencing mechanisms of geopolymer cemented granular materials: a dem study considering realistic particle shapes, Constr. Build. Mater. 509 (2026) 145237.
[15] T. Yu, J. Zhao, Semi-coupled resolved cfd-dem simulation of powder-based selective laser melting for additive manufacturing, Comput. Methods Appl. Mech. Eng. 377 (2021) 113707.
[16] Z. Lai, J. Zhao, S. Zhao, L. Huang, Signed distance field enhanced fully resolved cfd-dem for simulation of granular flows involving multiphase fluids and irregularly shaped particles, Comput. Methods Appl. Mech. Eng. 414 (2023) 116195.
[17] T. Yu, J. Zhao, GPU-optimized adaptive mesh refinement for scalable two-phase resolved CFD-dem simulations on unstructured hexahedral grids, Comput. Phys. Commun. 319 (2025) 109939.
[18] B.K. Cook, D.R. Noble, J.R. Williams, A direct simulation method for particle-fluid systems, Eng. Comput. 21 (2/3/4) (2004) 151–168.
[19] N. Younes, A. Wautier, R. Wan, O. Millet, F. Nicot, R. Bouchard, Dem-LBM coupling for partially saturated granular assemblies, Comput. Geotech. 162 (2023) 105677.
[20] S.F. Sizkow, U.E. Shamy, SPH-dem simulations of saturated granular soils liquefaction incorporating particles of irregular shape, Comput. Geotech. 134 (2021) 104060.
[21] W.-J. Xu, X.-Y. Dong, Simulation and verification of landslide tsunamis using a 3D SPH-dem coupling method, Comput. Geotech. 129 (2021) 103803.
[22] A.S. Baumgarten, B.L. Couchman, K. Kamrin, A coupled finite volume and material point method for two-phase simulation of liquid-sediment and gas-sediment flows, Comput. Methods Appl. Mech. Eng. 384 (2021) 113940.
[23] D. Sulsky, Z. Chen, H.L. Schreyer, A particle method for history-dependent materials, Technical Report, 1993.
[24] H. Chen, S. Zhao, J. Zhao, X. Zhou, Dem-enriched contact approach for material point method, Comput. Methods Appl. Mech. Eng. 404 (2023) 115814.
[25] J.N. Reddy, D.K. Gartling, The Finite Element Method in Heat Transfer and Fluid Dynamics, CRC press, 2010.
[26] Y.-F. Jin, Z.-Y. Yin, X.-W. Zhou, F.-T. Liu, A stable node-based smoothed pfem for solving geotechnical large deformation 2D problems, Comput. Methods Appl. Mech. Eng. 387 (2021) 114179.
[27] R.A. Gingold, J.J. Monaghan, Smoothed particle hydrodynamics: theory and application to non-spherical stars, Mon. Not. R. Astron. Soc. 181 (3) (1977) 375–389.
[28] C. Yang, F. Zhu, J. Zhao, Coupled total-and semi-lagrangian peridynamics for modelling fluid-driven fracturing in solids, Comput. Methods Appl. Mech. Eng. 419 (2024) 116580.
[29] C. Yang, F. Zhu, J. Zhao, A multi-horizon fully coupled thermo-mechanical peridynamics, J. Mech. Phys. Solids 191 (2024) 105758.
[30] C. Yang, J. Zhao, F. Zhu, Coupled thermo-hydrodynamic-mechanical peridynamics for thermal fluid-solid interactions with fracturing, J. Mech. Phys. Solids 208 (2025) 106492.
[31] H. Akbari, M.M. Namin, Moving particle method for modeling wave interaction with porous structures, Coastal Eng. 74 (2013) 59–73.
[32] A. Vaucorbeil, V.P. Nguyen, C.R. Hutchinson, A total-lagrangian material point method for solid mechanics problems involving large deformations, Comput. Methods Appl. Mech. Eng. 360 (2020) 112783.
[33] M. Molinos, P. Navas, M. Pastor, M.M. Stickle, On the dynamic assessment of the local-maximum entropy material point method through an explicit predictor-corrector scheme, Comput. Methods Appl. Mech. Eng. 374 (2021) 113512.
[34] G. Pretti, W.M. Coombs, C.E. Augarde, B. Sims, M.M. Puigvert, J.A.R. Gutiérrez, A conservation law consistent updated lagrangian material point method for dynamic analysis, J. Comput. Phys. 485 (2023) 112075.
[35] P.J. Baioni, T. Benacchio, L. Capone, C.D. Falco, Portable, massively parallel implementation of a material point method for compressible flows, Comput. Part. Mech. 12 (2024) 1–23.
[36] W.M. Coombs, R.E. Bird, G. Pretti, The aggregated material point method (AGMPM), Comput. Methods Appl. Mech. Eng. 442 (2025) 118012.
[37] W.M. Coombs, Ghost stabilisation of the material point method for stable quasi-static and dynamic analysis of large deformation problems, Int. J. Numer. Methods Eng. 124 (21) (2023) 4841–4875.
[38] W. Liang, K.-Y. He, Y.-F. Jin, Z.-Y. Yin, A gradient-smoothed material point method for reducing cell crossing noise in large deformation problems, Comput. Geotech. 169 (2024) 106169.
[39] H. Zhang, K. Wang, Z. Chen, Material point method for dynamic analysis of saturated porous media under external contact/impact of solid bodies, Comput. Methods Appl. Mech. Eng. 198 (17-20) (2009) 1456–1472.
[40] S. Kularathna, W. Liang, T. Zhao, B. Chandra, J. Zhao, K. Soga, A semi-implicit material point method based on fractional-step method for saturated soil, Int. J. Numer. Anal. Methods Geomech. 45 (10) (2021) 1405–1436.
[41] W. Liang, J. Zhao, H. Wu, K. Soga, Multiscale, Multiphysics modeling of saturated granular materials in large deformation, Comput. Methods Appl. Mech. Eng. 405 (2023) 115871.
[42] J. Yu, J. Zhao, W. Liang, S. Zhao, A semi-implicit material point method for coupled thermo-hydro-mechanical simulation of saturated porous media in large deformation, Comput. Methods Appl. Mech. Eng. 418 (2024) 116462.
[43] S. Bandara, K. Soga, Coupling of soil deformation and pore fluid flow using material point method, Comput. Geotech. 63 (2015) 199–214.
[44] K. Feng, D. Huang, G. Wang, Two-layer material point method for modeling soil-water interaction in unsaturated soils and rainfall-induced slope failure, Acta Geotech. 16 (8) (2021) 2529–2551.
[45] K.-Y. He, Y.-F. Jin, X.-W. Zhou, Z.-Y. Yin, A high-performance semi-implicit two-phase two-layer mpm framework for modeling granular mass-water interaction problems, Comput. Methods Appl. Mech. Eng. 427 (2024) 117064.
[46] Q.A. Tran, G. Grimstad, S.A.G. Amiri, MPMICE: a hybrid MPM-CFD model for simulating coupled problems in porous media. application to earthquake-induced submarine landslides, Int. J. Numer. Methods Eng. 125 (5) (2024) 7383.
[47] Y. Nakamichi, S. Sugie, T. Takeyama, A coupled mpm-sph numerical simulation for fully saturated soil, in: International Conference of the International Association for Computer Methods and Advances in Geomechanics, Springer, 2021, pp. 794–801.
[48] S. Pan, Y. Yamaguchi, A. Suppasri, S. Moriguchi, K. Terada, MPM-FEM hybrid method for granular mass-water interaction problems, Comput. Mech. 68 (1) (2021) 155–173.
[49] X. Sun, J. Wang, J. Mao, L. Wu, J. Zeng, H. Wei, D. Pan, Y. Li, Z. Guo, Evolution of the soil dynamic response during the vibratory pile driving based on an integrated MPM-FEM method, Comput. Part. Mech. 12 (2025) 1–23.
[50] H. Gotoh, A. Khayyer, On the state-of-the-art of particle methods for coastal and ocean engineering, Coastal Eng. J. 60 (1) (2018) 79–103.
[51] Y. Zhao, C. Jiang, J. Choo, Circumventing volumetric locking in explicit material point methods: a simple, efficient, and general approach, Int. J. Numer. Methods Eng. 124 (23) (2023) 5334–5355.
[52] R.M. Telikicherla, G. Moutsanidis, A displacement-based material point method for weakly compressible free-surface flows, Comput. Mech. 75 (2024) 1–17.
[53] B. Chandra, R. Hashimoto, S. Matsumi, K. Kamrin, K. Soga, Stabilized mixed material point method for incompressible fluid flow analysis, Comput. Methods Appl. Mech. Eng. 419 (2024) 116644.
[54] Z. Sun, Y. Hua, Y. Xu, X. Zhou, Simulation of fluid-structure interaction using the density smoothing b-spline material point method with a contact approach, Comput. Math. Appl. 176 (2024) 525–544.
[55] K.-Y. He, Y.-F. Jin, X.-W. Zhou, Z.-Y. Yin, X. Chen, A generalized projection algorithm for overcoming volumetric locking in explicit material point method, Comput. Geotech. 186 (2025) 107391.
[56] Z. Cheng, S. Zhao, H. Chen, J. Zhao, Stabilized explicit material point method for fluid flow and fluid-structure interaction simulations using dual high-order b-spline volume averaging, Comput. Methods Appl. Mech. Eng. 448 (2026) 118428.
[57] E.A.D.S. Neto, D. Peric, D.R. Owen, Computational Methods for Plasticity: Theory and Applications, John Wiley & Sons, 2008.
[58] W.M. Coombs, T.J. Charlton, M. Cortis, C.E. Augarde, Overcoming volumetric locking in material point methods, Comput. Methods Appl. Mech. Eng. 333 (2018) 1–21.

[59] A.S. Baumgarten, K. Kamrin, Analysis and mitigation of spatial integration errors for the material point method, Int. J. Numer. Methods Eng. 124 (11) (2023) 2449–2497.
[60] F. Zhang, X. Zhang, K.Y. Sze, Y. Lian, Y. Liu, Incompressible material point method for free surface flow, J. Comput. Phys. 330 (2017) 92–110.
[61] S. Kularathna, K. Soga, Implicit formulation of material point method for analysis of incompressible materials, Comput. Methods Appl. Mech. Eng. 313 (2017) 673–686.
[62] J. Yu, J. Zhao, K. Soga, S. Zhao, W. Liang, A fully coupled THMC-MPM framework for modeling coupled phase transition and large deformation in methane hydrate-bearing sediment, J. Mech. Phys. Solids 206 (2025) 106368.
[63] W. Liang, B. Chandra, J. Yu, Z.-Y. Yin, J. Zhao, A total-lagrangian material point method for fast and stable hydromechanical modeling of porous media, Int. J. Numer. Methods Eng. 126 (19) (2025) 70135.
[64] L. Moreno, R. Wuechner, A. Larese, A mixed stabilized mpm formulation for incompressible hyperelastic materials using variational subgrid-scales, Comput. Methods Appl. Mech. Eng. 435 (2025) 117621.
[65] J. Yu, W. Liang, J. Zhao, Enhancing dynamic modeling of porous media with compressible fluid: a thm material point method with improved fractional step formulation, Comput. Methods Appl. Mech. Eng. 444 (2025) 118100.
[66] B. Chandra, R. Hashimoto, K. Kamrin, K. Soga, Mixed material point method formulation, stabilization, and validation for a unified analysis of free-surface and seepage flow, J. Comput. Phys. 519 (2024) 113457.
[67] Z.-P. Chen, X. Zhang, K.Y. Sze, L. Kan, X.-M. Qiu, VP material point method for weakly compressible problems Comput. Fluids 176 (2018) 170–181.
[68] X.-W. Zhou, Y.-F. Jin, K.-Y. He, Z.-Y. Yin, F.-T. Liu, A novel implicit fem-mpm coupling framework using convex cone programming for elastoplastic problems, Comput. Methods Appl. Mech. Eng. 429 (2024) 117153.
[69] X.-W. Zhou, Y.-F. Jin, K.-Y. He, Z.-Y. Yin, An improved explicit MPM formulation and its coupling scheme with fem, Comput. Methods Appl. Mech. Eng. 436 (2025) 117734.
[70] H. Chen, S. Zhao, J. Zhao, A sparse-memory-encoding GPU-MPM framework for large-scale simulations of granular flows, Comput. Geotech. 180 (2025) 107113.
[71] X. Zheng, F. Pisano, P.J. Vardon, M.A. Hicks, An explicit stabilised material point method for coupled hydromechanical problems in two-phase porous media, Comput. Geotech. 135 (2021) 104112.
[72] D. Wang, B. Wang, W. Yuan, L. Liu, Investigation of rainfall intensity on the slope failure process using GPU-accelerated coupled mpm, Comput. Geotech. 163 (2023) 105718.
[73] A.S. Baumgarten, K. Kamrin, A general fluid-sediment mixture model and constitutive theory validated in many flow regimes, J. Fluid Mech. 861 (2019) 721–764.
[74] Y. Zhang, C. Liu, A unified numerical framework for the soil and fluid coupling problem considering mixture and separation, Comput. Geotech. 186 (2025) 107373.
[75] C. Mast, P. Mackenzie-Helnwein, P. Arduino, G.R. Miller, W. Shin, Mitigating kinematic locking in the material point method, J. Comput. Phys. 231 (16) (2012) 5351–5373.
[76] C.M. Mast, P. Arduino, P. Mackenzie-Helnwein, G.R. Miller, Simulating granular column collapse using the material point method, Acta Geotech. 10 (1) (2015) 101–116.
[77] M. Xie, P. Navas, S. López-Querol, An implicit locking-free b-spline material point method for large strain geotechnical modelling, Int. J. Numer. Anal. Methods Geomech. 47 (15) (2023) 2741–2761.
[78] M. Xie, P. Navas, S. López-Querol, A stabilised semi-implicit double-point material point method for soil-water coupled problems, Comput. Part. Mech. 12 (5) (2025) 1–31.
[79] M. Koßler, S. Maassen, R. Niekamp, J. Schröder, Reduction of stress oscillations in the material point method based on the random grid-shift technique, Comput. Part. Mech. 12 (5) (2025) 1–18.
[80] J. Fern, A. Rohe, K. Soga, E. Alonso, The material point method for geotechnical engineering: a practical guide, CRC Press, 2019.
[81] S. Ergun, A.A. Orning, Fluid flow through randomly packed columns and fluidized beds, Ind. Eng. Chem. 41 (6) (1949) 1179–1184.
[82] J. Kozeny, Ueber kapillare leitung des wassers im boden, Sitzungsberichte der Akademie der Wissenschaften in Wien 136 (1927) 271.
[83] P.C. Carman, Fluid flow through granular beds, Chem. Eng. Res. Des. 75 (1997) 32–S48.
[84] P. Menetrey, K.J. Willam, Triaxial failure criterion for concrete and its generalization, Struct. J. 92 (3) (1995) 311–318.
[85] F.H. Harlow, The particle-in-cell computing method for fluid dynamics, Methods Comput. Phys. 3 (1964) 319–343.
[86] J.U. Brackbill, H.M. Ruppel, Flip: a method for adaptively zoned, particle-in-cell calculations of fluid flows in two dimensions, J. Comput. Phys. 65 (2) (1986) 314–343.
[87] C. Jiang, C. Schroeder, A. Selle, J. Teran, A. Stomakhin, The affine particle-in-cell method, ACM Trans. Graphics (TOG) 34 (4) (2015) 1–10.
[88] C. Fu, Q. Guo, T. Gast, C. Jiang, J. Teran, A polynomial particle-in-cell method, ACM Trans. Graphics (TOG) 36 (6) (2017) 1–12.
[89] Y. Fei, Q. Guo, R. Wu, L. Huang, M. Gao, Revisiting integration in the material point method: a scheme for easier separation and less dissipation, ACM Trans. Graphics (TOG) 40 (4) (2021) 1–16.
[90] Y. Zhao, M. Li, C. Jiang, J. Choo, Mapped material point method for large deformation problems with sharp gradients and its application to soil-structure interactions, Int. J. Numer. Anal. Methods Geomech. 48 (9) (2024) 2334–2355.
[91] L. Blatny, J.M. Gray, J. Gaume, A critical state μ (I)-rheology model for cohesive granular flows, J. Fluid Mech. 997 (2024) 67.
[92] C. Coetzee, The mAterial Point Method: Theoretical Formulation, Implementation and Analysis version 1.1.
[93] Y. Gan, Z. Sun, Z. Chen, X. Zhang, Y. Liu, Enhancement of the material point method using b-spline basis functions, Int. J. Numer. Methods Eng. 113 (3) (2018) 411–431.
[94] S.G. Bardenhagen, E.M. Kober, et al., The generalized interpolation material point method, Comput. Model. Eng. Sci. 5 (6) (2004) 477–496.
[95] A. Sadeghirad, R.M. Brannon, J. Burghardt, A convected particle domain interpolation technique to extend applicability of the material point method for problems involving massive deformations, Int. J. Numer. Methods Eng. 86 (12) (2011) 1435–1456.
[96] M.G. Cox, The numerical evaluation of b-splines,, IMA J. Appl. Math. 10 (2) (1972) 134–149.
[97] A.D. Vaucorbeil, V.P. Nguyen, S. Sinaie, J.Y. Wu, Material point method after 25 years: theory, implementation, and applications, Adv. Appl. Mech. 53 (2020) 185–398.
[98] R.M. Telikicherla, G. Moutsanidis, Treatment of near-incompressibility and volumetric locking in higher order material point methods, Comput. Methods Appl. Mech. Eng. 395 (2022) 114985.
[99] Y. Yue, B. Smith, C. Batty, C. Zheng, E. Grinspun, Continuum foam: a material point method for shear-dependent flows, ACM Trans. Graphics (TOG) 34 (5) (2015) 1–20.
[100] R. Xu, P. Stansby, D. Laurence, Accuracy and stability in incompressible SPH (ISPH) based on the projection method and a new approach, J. Comput. Phys. 228 (18) (2009) 6703–6725.
[101] F. Zhang, X. Zhang, K.Y. Sze, Y. Liang, Y. Liu, Improved incompressible material point method based on particle density correction, Int. J. Comput. Methods 15 (07) (2018) 1850061.
[102] C. Yang, J. Zhao, F. Zhu, R. Feng, A multi-horizon peridynamics for coupled fluid flow and heat transfer, J. Fluid Mech. 1010 (2025) 66.
[103] R. Courant, K. Friedrichs, H. Lewy, On the partial difference equations of mathematical physics, IBM J. Res. Dev. 11 (2) (1967) 215–234.
[104] S. Kularathna, Splitting Solution Scheme for Material Point Method, Technical Report, University of Cambridge, 2018. Ph.D. thesis.
[105] K. Terzaghi, Theoretical Soil Mechanics, 1943.
[106] J. Mandel, Consolidation des sols (étude mathématique) Geotechnique 3 (7) (1953) 287–299.
[107] C. Cryer, A comparison of the three-dimensional consolidation theories of biot and terzaghi, Q. J. Mech. Appl. Math. 16 (4) (1963) 401–412.
[108] D. Mason, A. Solomon, L. Nicolaysen, Evolution of stress and strain during the consolidation of a fluid-saturated porous elastic sphere, J. Appl. Phys. 70 (9) (1991) 4724–4740.

[109] M. Kurashige, K. Sato, K. Imai, Mandel and cryer problems of fluid-saturated foams with negative poisson's ratio, Acta. Mech. 175 (2005) 25–43.
[110] A. H-, D. Cheng, Poroelasticity, 27, Springer, 2016.
[111] E. Daly, S. Grimaldi, H.H. Bui, et al, Explicit incompressible sph algorithm for free-surface flow modelling: a comparison with weakly compressible schemes, Adv. Water Resour. 97 (2016) 156–167.
[112] X. Zhang, E.O. nate, S.A.G. Torres, J. Bleyer, K. Krabbenhoft, A unified lagrangian formulation for solid and fluid dynamics and its possibility for modelling submarine landslides and their consequences, Comput. Methods Appl. Mech. Eng. 343 (2019) 314–338.
[113] E. Lajeunesse, J. Monnier, G. Homsy, Granular slumping on a horizontal surface, Phys. Fluids 17 (10) (2005) 103302.
[114] L. P, F. Liu, P. Lin, K.-A. Chang, T. Sakakiyama, Numerical modeling of wave interaction with porous structures, J. Waterw. 125 (6) (1999) 322–330.
[115] Y.-F. Jin, Z.-Y. Yin, X.-W. Zhou, Two-phase two-layer SNS-PFEM for hydromechanical geotechnical large deformation problems, Comput. Methods Appl. Mech. Eng. 418 (2024) 116542.
[116] S.A. Rzadkiewicz, C. Mariotti, P. Heinrich, Numerical simulation of submarine landslides and their hydraulic effects, J. Waterw. Port Coastal Ocean Eng. 123 (4) (1997) 149–157.
[117] C. Zhu, C. Peng, W. Wu, C. Wang, A multi-layer sph method for generic water-soil dynamic coupling problems. part i: revisit, theory, and validation, Comput. Methods Appl. Mech. Eng. 396 (2022) 115106.
[118] K.-L. Zhao, L.C. Qiu, Y. Liu, Numerical study of water wave generation by granular-liquid mixture collapse using two-phase material point method, Appl. Ocean Res. 137 (2023) 103608.
[119] B. Spinewine, H. Capart, Intense bed-load due to a sudden dam-break, J. Fluid Mech. 731 (2013) 579–614.
[120] J.-Y. Chen, J. Zhao, R.-F. Feng, R.-C. Ni, C. Peng, GPU-accelerated multi-material FVM-SPH with immersed boundary method for high-fidelity modeling of shock-structure interactions, Comput. Mech. 77 (2025) 1–23.